

Copyright

By

Behdad Aminzadeh Goharrizi

2009

Thesis committee for Behdad Aminzadeh Goharrizi certifies that this is the approved version of the following thesis

The Transition between Sharp and Diffusive Wetting Fronts as a Function of Imbibing Fluid properties

Approved by

Supervising Committee:

David DiCarlo, Supervisor

Larry Lake, Reader

The Transition between Sharp and Diffusive Wetting Fronts as a Function of Imbibing Fluid Properties

By

Behdad Aminzadeh Goharrizi

THESIS

Presented to the Faculty of the Graduate School of

The University of Texas at Austin

in Partial Fulfillment

of the Requirements

for the Degree of

Master of Science in Engineering

The University of Texas at Austin

December 2009

Dedication

To

my wife, Elham Barkhordari

without whose supports none of this would be possible

Acknowledgements

I am extremely thankful to my supervisor, Dr. David DiCarlo for his supervision, support, and friendship during this research. Without his patience, perpetual energy and enthusiasm in research, this work would have never happened. I thank the fellows in our research group, in particular Hassan Dehghanpour and Mohammad Mirzaei for his collaboration in the development of this scientific study. I also thank Mandana Ashouri, Sheel Vyas, and Hans-Paul Anguillet for experimental assistance.

December 2009

Abstract

The Transition between Sharp and Diffusive Wetting Fronts as a Function of Imbibing Fluid properties

Behdad Aminzadeh Goharrizi, M.S.E

The University of Texas at Austin, 2009

Supervisor: David DiCarlo

The efficiency of one fluid displacing another in a permeable medium depends on the pore-scale dynamics at the main wetting front. Experiments have shown that the frontal dynamics can result in two different flow regimes: a sharp and a diffuse front. In the sharp front regime, the displacing fluid occupies nearly all the pores and throats behind the main wetting front and the saturation changes abruptly. In contrast, in the diffuse front regime, pores are filled gradually at the main wetting front, and the saturation change is gradual in space. The different fronts can greatly alter the relative permeability curves, the trapping mechanisms, and the displacement efficiency.

Directly measuring the sharpness of the front is difficult. Instead, here we correlate the front sharpness to saturation overshoot, which occurs for moderate to high flux vertical displacements of low density fluid by a higher density fluid in 1-D homogeneous permeable media.

We hypothesize the sharpness of wetting front can be explained by competition between two different pore - filling mechanisms (called snap-off and piston-like) with the competition controlled by the velocity of the front and thus the injected flux. We conduct series of infiltration experiments to determine the saturation profile as a function of flux for seven different fluids. We find that for each fluid there is a flux (called overshoot flux) below which saturation overshoot ceases and the front is diffuse. We find that the overshoot flux depends inversely on the invading fluid's viscosity, and shows little or no dependence on the invading fluid's surface tension, vapor pressure, and its miscibility with water.

Table of Contents

Acknowledgments	v
Abstract	vi
Table of Contents	viii
List of Tables	x
List of Figures	xi
Chapter 1: Introduction.....	1
Chapter 2: Theoretical background	7
2 - 1 Pore Scale Displacement	8
2 - 2 Capillary Desaturation Curve.....	12
2 - 3 Pore Doublet Model.....	13
2 - 4 Stability Analysis.....	16
2 - 5 Preferential Flow and Saturation Overshoot.....	20
2 - 6 Sharp and Diffuse Front.....	24
Chapter 3: Materials and Methods.....	27
Chapter 4: Results and Discussion	32
4 - 1: Experimental Results	32
4 - 2: Theoretical Evidence.....	44
4 - 3: Discussion.....	47
4 - 4: Proposed Model.....	59

Chapter 5: Summary and Conclusion.....	63
Nomenclature	65
Acronyms	66
References.....	67
Vita.....	70

List of Tables

Table 2 - 1 Saffman – Taylor instability criteria for a sharp front [<i>Saffman and Taylor</i> , 1958].....	20
Table 3 - 1 Physical parameters for the four sands used in the study [<i>Schroth et al.</i> , 2003].....	28
Table 3 - 2 Physical properties of fluids used in this study.....	29
Table 4 - 1 Measured overshoot flux, transition flux, and tip length.....	42

List of Figures

Figure 1 - 1 Diffuse front (a) observed at low flux and sharp front (a) observed at high flux of injecting fluid in 2 D micro model of Lenormand and Zarcone. [1984].....	1
Figure 1 - 2: Schematic capillary desaturation curve. [Lake 1989].....	3
Figure 1 - 3 Cartoon of a saturation overshoot and the associated saturation within the flow path. Saturation overshoot occurs when the tip saturation is greater than the tail saturation.....	5
Figure 2 - 1 Typical drainage curve as a function of saturation.....	9
Figure 2 - 2 Schematic diagram of the network model in the immiscible displacement..	10
Figure 2 - 3 Typical imbibition curve as a function of saturation.....	10
Figure 2 - 4 In the snap off process water layer develops as capillary pressure decrease.....	11
Figure 2 - 5 Schematic diagram of pore doublet model (a) before trapping, (b) after trapping [Lake 1989].....	14
Figure 2 - 6 Schematic diagram of vertical displacement of phase 2 by phase 1.....	17
Figure 2 - 7 Perturbed interface, it can happen in the real media because of the micro heterogeneity	18
Figure 2 - 8 Formation of soil water fingers. Photo was taken in Port Campbell National Park, 60 km east of Warrnambool, Australia. [Stagnitti et al., 1998].....	21
Figure 2 - 9 Schematic of a sharp front and the associated water saturation within the flow path. Saturation over shoot occurs when the tip saturation is greater than the tail saturation.....	22

Figure 2 - 10 Network model sharp and diffuse front and the corresponding relative permeability curves. [Hughes and Blunt, 2001]	25
Figure 3 - 1 Photograph of the spherical grains of the 12/20 sand. [DiCarlo 2004].....	28
Figure 3 -2 Schematic diagram of apparatus used in this study.....	30
Figure 4 - 1 Snapshots of the ethanol saturation profile versus depth for four different applied fluxes. From top to bottom fluxes are 5.83×10^{-4} m/s, 2.33×10^{-4} m/s, 4.66×10^{-5} m /s and the lowest flux is 2.33×10^{-6} m/s. The tip and tail saturation decrease when the injected flux is decreased.....	33
Figure 4 -2 Measured tip and tail saturation as a function of flux for ethanol. Three regions can be identified. The overshoot flux marks the onset of overshoot, and is equal to 2.05×10^{-6} m/s.....	34
Figure 4 - 3 Measured tip and tail saturation as a function of flux for methanol. Methanol has an overshoot flux of 8.33×10^{-6} m / s.....	36
Figure 4 - 4 Measured tip and tail saturation as a function of flux for iso – propanol. Iso – propanol has an overshoot flux of 1.96×10^{-6} m / s.....	37
Figure 4 - 5 Measured tip and tail saturation as a function of flux for hexane. Hexane has an overshoot flux of 1.13×10^{-5} m / s.....	38
Figure 4 - 6 Measured tip and tail saturation as a function of flux for octane. Octane has an overshoot flux of 6.16×10^{-6} m / s.....	38
Figure 4 - 7 Measured tip and tail saturation as a function of flux for decane. Decane has an overshoot flux of 3.68×10^{-6} m / s.....	39
Figure 4 - 8 Measured tip and tail saturation as a function of flux for water with 30 / 40 sands. It shows an overshoot flux of 2.13×10^{-6} m / s. [DiCarlo, 2004]....	40

Figure 4 - 9 Measured tip and tail saturation as a function of flux for water with 12 / 20 sands. It shows an overshoot flux of 1.67×10^{-7} m / s. [*DiCarlo*, 2004].... 40

Figure 4 - 10 Measured tip and tail saturation as a function of flux for water with 20 / 30 sands. It shows an overshoot flux of 5.45×10^{-7} m / s. [*DiCarlo*, 2004].... 41

Figure 4 - 11 Measured tip and tail saturation as a function of flux for water with 50 / 70 sands. It shows an overshoot flux of 1.67×10^{-5} m / s. [*DiCarlo*, 2004].... 42

Figure 4 - 12 Saturation profile as a function of η , Richard's equation is inadequate of describing the fluid behavior if Δs is higher than snap off saturation.....44

Figure 4 - 13: Measured overshoot flux versus viscosity for all fluids both alcohols and alkenes. The overshoot flux shows an inverse dependence on viscosity.....48

Figure 4 - 14 Measured overshoot flux as a function of surface tension / viscosity. It shows a linear relationship, except for water, between overshoot flux and surface tension / viscosity.....51

Figure 4 - 15 Measured overshoot flux as a function of surface tension. It shows overshoot flux is independent of surface tension.....51

Figure 4 - 16 Measured overshoot flux as a function of surface tension / viscosity. It shows overshoot flux is independent of surface tension.....52

Figure 4 - 17 Measured overshoot flux as a function of vapor pressure for all fluids both alcohols, alkenes and water. There is a weak dependence between vapor pressure and overshoot flux.....53

Figure 4 - 18 Measured overshoot flux as a function calculated overshoot flux. The vapor transport model underestimates experimental behavior.....55

Figure 4 - 19 Measured overshoot flux as a function of density / viscosity for all fluids both alcohols, alkenes and water. There is a weak dependence between density / viscosity and overshoot flux.....56

Figure 4 - 20 Measured overshoot flux as a function of grain size for water. There is a linear dependence in log – log plot for overshoot flux as a function of grain size. Overshoot flux scale as D^{-3} 57

Figure 4 - 21 Measured overshoot flux and hydraulic conductivity of water as a function of grain size. The intersection of these two lines is at 0.108 mm and predicts the overshoot flux as 0.186×10^{-4} 58

Figure 4 - 22 Measured tip length as a function of surface tension / density for all fluids: alcohols, alkanes and water. The tip length was measured from the infiltration front to where the saturation is halfway between its initial value and the tail value. There is a linear dependence between tip length and surface tension / density.....59

Figure 4 - 23 Flow through a triangular duct with constant cross-section area.....59

Figure 4 - 24 Flow through a Layer ahead of the main wetting front60

Figure 4 - 25 Estimated saturation ahead of the main wetting front for water in 30 / 40 sand.....62

Chapter 1: Introduction

When a wetting fluid imbibes into a permeable medium displacing the nonwetting phase, the dynamics at the initial wetting front can have large effects on the overall displacement. For simplicity, we follow the early micromodel experiments of Lenormand and Zarcane [1984] and define two flow regimes, a diffuse wetting front and a sharp wetting front. In the sharp front regime, the displacing fluid occupies nearly all the pores and throats behind the main wetting front and the saturation changes abruptly. In contrast, in the diffuse regime, pores are filled gradually at the main wetting front, and the saturation change is gradual in space. The different fronts can greatly alter the relative permeability curves, the trapping mechanisms, and the displacement efficiency.

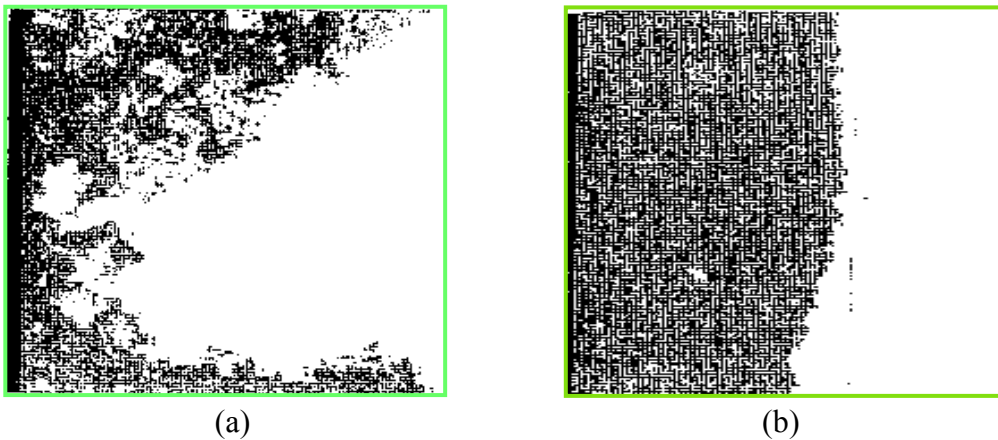


Figure 1-1 Diffuse front (a) observed at low flux and sharp front (a) observed at high flux of injecting fluid in 2 D micro model of Lenormand and Zarcane. [1984]

The micromodel experiments (Fig. 1 - 1) show that the diffuse wetting front occurs at very low displacement velocities when capillary forces are dominant. The wetting phase then fills the smallest accessible spaces with little regard to the main front, leading to a gradual increase of saturation at the wetting front.

In contrast, sharp fronts are observed when the front velocity is increased and viscous pressure drops compete with the capillary forces [Lenormand *et al.*, 1988]. This greatly reduces the amount of accessible pore space, causing the pore filling to be much more compact leading to an abrupt increase of saturation at the wetting front. Whether or not a diffuse or sharp front occurs at the pore scale can have large effects on an overall displacement, as this physics has been implicated in controlling the shape of the capillary desaturation curve (CDC) [Lenormand *et al.*, 1988], changes in the relative permeability [Hughes and Blunt, 2001; Mogensen and Stenby, 1998], and flow stability [DiCarlo, 2004; 2006; 2007].

In particular, many enhanced oil recovery (EOR) techniques have the goal of reducing the nonwetting phase residual saturation (S_{or}) by using the capillary desaturation curve (CDC). A textbook CDC is depicted in Figure 1 – 2. The x-axis consists of the capillary number which is a dimensionless number given by,

$$N_{Ca} = \frac{\mu v}{\sigma} \quad (1 - 1)$$

where v is the front velocity, μ is the viscosity of the wetting phase, and σ is the interfacial tension. The capillary number is related to the ratio of the viscous forces (which scale as $v\mu$) to the capillary forces (which scale as σ) at the pore scale. The y-axis is the non-wetting phase residual saturation (S_{or}). Below a critical capillary number the residual nonwetting phase is constant. Above the critical capillary number the residual saturation decreases with increasing capillary number until reaching a very low (or zero) value at capillary numbers around 10^{-2} to 10^{-1} .

It is typically assumed that the capillary number is the controlling parameter for the residual saturation. If capillary forces dominate (below the critical capillary number), the front is diffuse and the nonwetting phase will be trapped in disconnected blobs and ganglia through capillary forces. At high capillary numbers the viscous drag creates pressure drops that sharpen the wetting front and prevent the capillary trapping. Thus the pore-scale dynamics of the initial wetting front play a crucial role in the overall displacement.

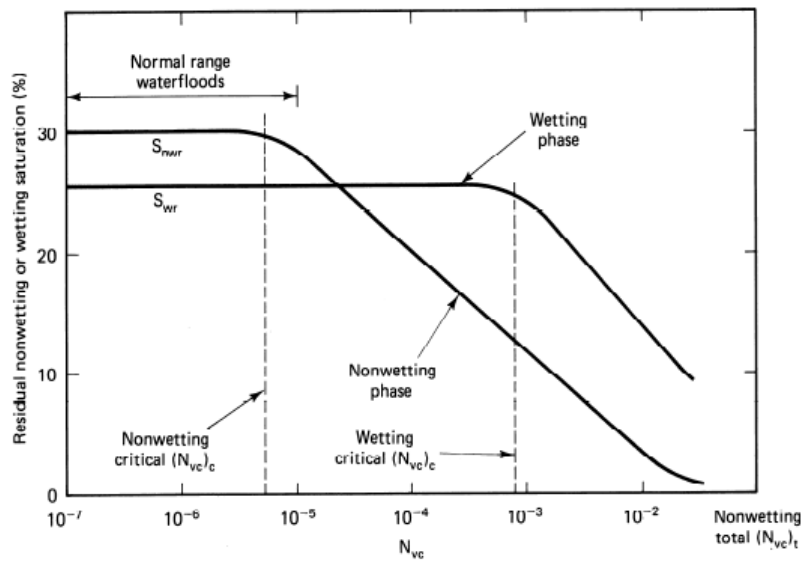


Figure 1 – 2 Schematic capillary desaturation curve [Lake 1989]

Measurements and observations of the front dynamics are crucial to resolving the transition to these two regimes. As mentioned above, Lenormand and Zarcone [1984] observed the two regimes in a 2D micromodel and related the regimes to the capillary number. Hughes and Blunt [2001] observe the same behavior in their network model, they also calculated the relative permeabilities and observed that the not only the residual oil saturation but also the relative permeabilities are functions of flow regimes.

Subsequently, Lu et al. [1994a; b], observed the two regimes in a 3D permeable medium, but only by looking at the edge of the permeable medium. This is necessary for visual

observations (as one cannot “see” inside of a 3D permeable medium), but the pores between the grains and the container walls are much different than the pores in the bulk.

Micro-tomography [*Alvarado et al.*, 2004; *Culligan et al.*, 2006; *Wildenschild et al.*, 2005] holds out promise for observing inside a permeable medium, and much work has been done on static snapshots of the positions of the grains and the fluid-fluid interfaces, but tomography is far from being fast enough to observe the moving front. Other techniques that can possibly observe pore filling in 3D permeable media, such as acoustic methods [*DiCarlo, et.al.* 2003] or index matched permeable media [*Stohr et al.*, 2003] are still being developed. Instead, it is possible and useful to observe this transition from macroscopic observations.

One macroscopic manifestation of the pore scale filling is saturation overshoot in 1D gravity driven flows. Vertical displacement of low density fluid by a higher density one in 1D homogenous permeable medium is known to create non-monotonic saturation profiles under certain boundaries and initial conditions [*DiCarlo*, 2004; 2007; *Geiger and Durnford*, 2000; *Stonestrom and Akstin*, 1994]. The schematic diagram of saturation overshoot is shown in Fig. 1 – 3.

These saturation profiles exhibits a high saturation at the front (hereafter called the tip) followed by a low saturation behind the front (hereafter called the tail), and is also known as saturation overshoot.

We hypothesize that different pore filling mechanisms dominate below and above the overshoot flux. At low frontal velocities, the wetting phase has time to establish and move through wetting layers ahead of the main wetting front. This provides the wetting phase access to pores a large distance ahead of the main wetting front, and then capillary

forces determine which of these pores fill. The sizable layers allow both snap-off filling mechanisms (where the wetting phase fills a pore or throat from the swelling of the layers) ahead of the front, and piston-like invasion percolation mechanisms at the front [Blunt and Scher, 1995]. As there is a range of pore and throat sizes and available filling mechanisms, this leads to a spatially diffuse front, and on a macro-scale, a relatively smooth increase of the saturation at the front. With this smooth increase, saturation overshoot does not occur and continuum based models are appropriate to describe the infiltration behavior.

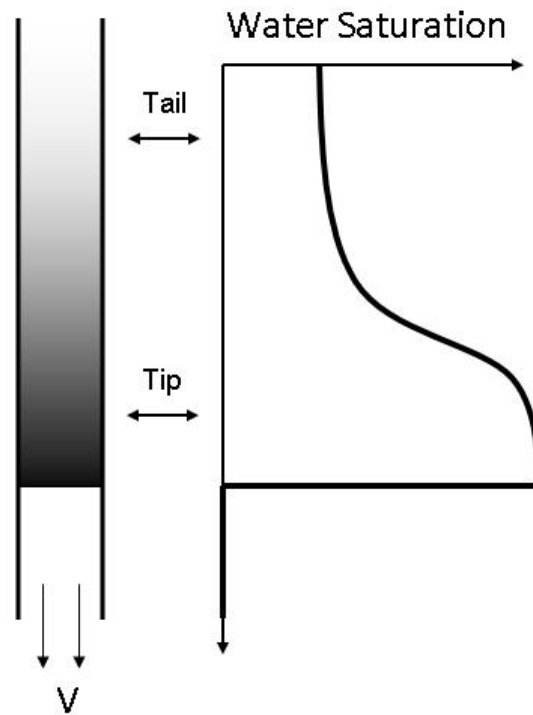


Figure 1 – 3 Cartoon of a saturation overshoot and the associated saturation within the flow path. Saturation overshoot occurs when the tip saturation is greater than the tail saturation.

In contrast, as the speed of the wetting front increases, the formation of wetting layers and wetting phase flow through these layers is suppressed relative to flow at the main wetting front. Not only the spatial range of available pores and throats is lessened, but

also the thinner or absent layers greatly suppress the snap-off filling mechanism [Lenormand *et al.*, 1988]. This leaves only the piston-like invasion percolation filling mechanism at the main wetting front. But since the piston-like mechanism is collective for imbibition, i.e. if one pore fills it makes it more likely for its neighbor to fill, this can cause excess pores to be filled, and in turn saturation overshoot. This suppression of snap-off will occur if the front is sharp at the pore scale. This is roughly the same mechanism which has been proposed to explain the capillary desaturation curve, where the residual non-wetting fluid is lowered with increasing capillary number due to the suppression of snap-off. [Lake, 1989]

In this work, we use saturation overshoot to study the dynamics at the initial wetting front as a function of imbibing fluid properties. We perform overshoot measurements as a function of flux for six different non-aqueous liquids, three alkanes (hexane, octane, and decane) and three alcohols (methanol, ethanol, and propanol). These liquids give us a range of molecular weights, viscosities, vapor pressures, and miscibility with the initial adsorbed water on the grain surfaces. We measure the flux above which the infiltrations exhibit overshoot, and corresponds this “overshoot” flux to the pore filling mechanism for each fluid. We find that for a particular permeable medium the overshoot flux shows only a dependence on the viscosity of the fluid, thus showing that along with capillarity, the viscosity plays a crucial role in the pore-filling dynamics at the wetting front.

Chapter 2: Theoretical Background

Immiscible displacement of a nonwetting fluid by a wetting one in permeable media is encountered in different fields such as oil production, ground water remediation, and soil and water contamination by organic pollutants. Over the past decades, numerous works have been conducted on multi phase flow through the permeable media [Lake, 1989; Eliassi and Glass, 2001; van Duijn et al., 2004; Cueto-Felgueroso and Juanes, 2009; DiCarlo, 2004; DiCarlo, 2005; DiCarlo et al., 2008; Eliassi and Glass, 2001; 2002; 2003; van Duijn et al., 2004].

“Vertical displacement of water in to the homogenous permeable media has been shown to produce preferential flow paths under certain boundary and initial conditions and media properties” [DiCarlo, 2004]. Preferential flow refers to the uneven and rapid movement of displacing fluid through the permeable medium. Preferential flow describes three different processes. Macro pore, funnel flow, and finger flow. In macro pore, displacing fluid passes through the high permeability routes caused by roots and worms. Funnel flow is referred to as a preferred pass of displacing fluid due to impermeable layer. Finger flow refers to instability of the interface when a higher density fluid (e.g. water) displaces a lower density fluid (e.g. air) at low velocities.

In this chapter, different process of fluid movement is explained followed by analyzing the different forces affecting the displacement efficiency. In addition, we use the perturbation theory to analyze the instability of a sharp and diffuse front when one phase invades another one.

2 – 1: Pore Scale Displacement processes:

Wettability is defined as the preference of a solid to contact one phase rather than the others. The wetting phase will spread out on the rock surface while the non-wetting phase stays in the middle of the pores. Rocks can be water-wet, oil-wet or intermediate-wet. Wettability could affect relative permeability, residual saturation, and saturation profiles in the immiscible displacement processes. The pore filling mechanisms, whether the non-wetting phase displaces the wetting phase or the wetting phase displaces the non-wetting phase, are different.

In this section, we try to briefly explain the different immiscible displacement process and the pore filling mechanism correspond to each of these processes.

In the immiscible displacement, if the permeable medium is initially saturated with a wetting fluid, the process is called *drainage*. The process by which the wetting fluid displaces a non wetting fluid is called *imbibition*. Since, the wetting fluid tend to flow impulsively therefore, this process is spontaneous.

Now, consider an immiscible displacement, if this process is done slowly, we can assume a series of fluid configuration at the capillary equilibrium. Measuring the capillary pressure (the difference between nonwetting phase and wetting phase pressure) as a function of saturation in the drainage processes results in drainage curve which is shown in figure 2 – 1.

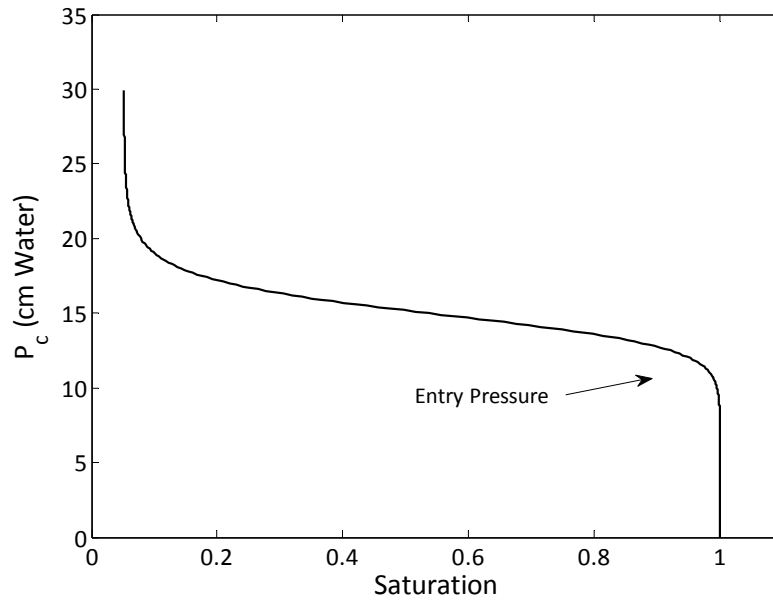


Figure 2 - 1 Typical drainage curve as a function of saturation.

Figure 2 – 2 shows a simplified permeable medium which is just an array of pores and throats (network model). Non-wetting fluid enters the permeable medium at the lowest capillary pressure or through the largest throat as shown in the figure 2 – 1. This capillary pressure is called entry pressure, which is the minimum capillary pressure required for a nonwetting phase to invade in to a wetting phase.

Capillary entry pressure can be calculated from the Eq. 2 - 1

$$P_c = \frac{2\sigma}{r_{t,\max}} \cos \theta \quad (2 - 1)$$

where the $r_{t,\max}$ is the biggest throat radius,. “As soon as the interface crosses the smallest radius in the throat (r_t) the non–wetting fluid will quickly fill the adjacent pore”. [DiCarlo, 2007]

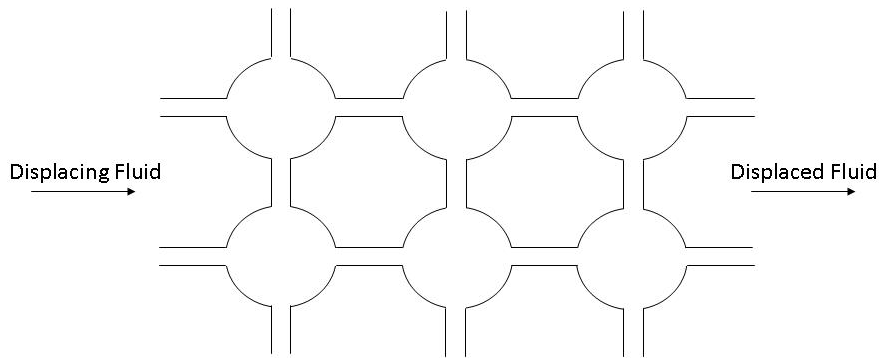


Figure 2 – 2 Schematic diagram of the network model in the immiscible displacement

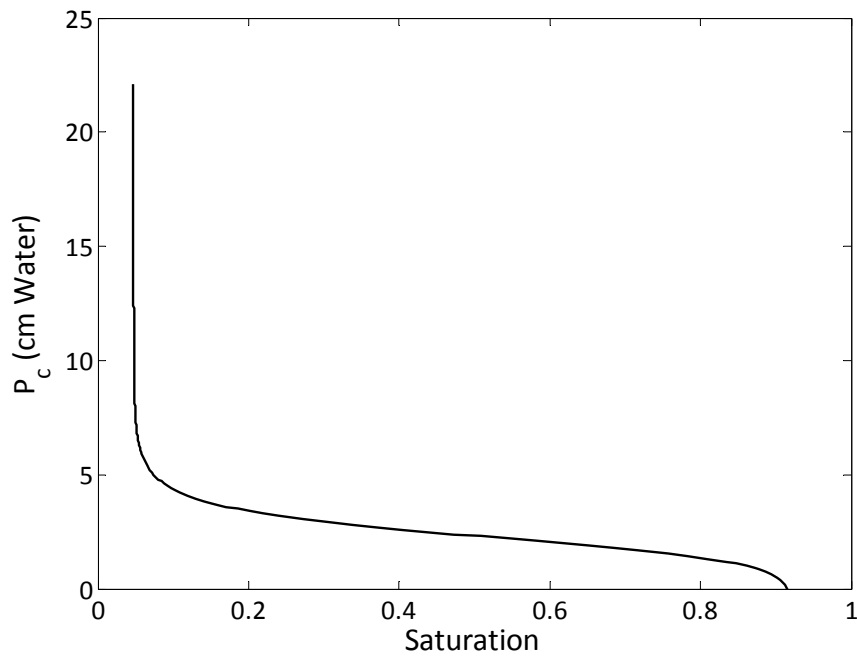


Figure 2 - 3 Typical imbibition curve as a function of saturation.

This process is called invasion percolation. If a throat fills, all adjacent pores will fill, but a throat can not fill until an adjacent pore is filled.

The non-wetting phase can not spread out on the rock surface, and the wetting phase will remain in the crevices. By increasing the pressure not only all pores will fill with the non-wetting saturation, but also the wetting phase layer in the crevices will decrease.

However, in the imbibition process by decreasing the capillary pressure the wetting phase (water) will displace the non – wetting phase (oil). Figure 2 – 3 shows the capillary a typical capillary pressure saturation curve in imbibition. The wetting phase invades the smallest portion of the pores. In this process throats will fill first and later the pores. In imbibition wetting phase water fills the pores with two different mechanisms, snap – off and piston like. These two pore filling mechanisms are the main factor to control the flow regime

Snap – off: Consider a throat with a square cross section, as shown in Fig. 2 -4, by decreasing the capillary pressure, water will flow to the throat through the corners; Therefore, the radius of the interface curvature increases. As soon as, the water in the corners comes in contact, the throat will fill completely, since the curvature radius is no longer able to increase

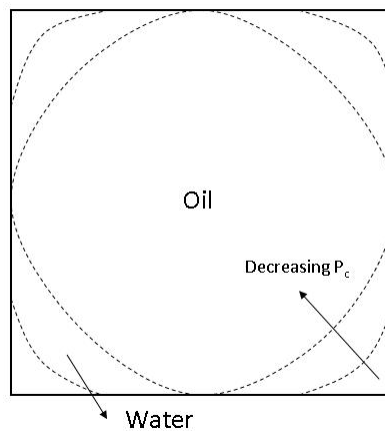


Figure 2 – 4 In the snap off process water layer develops as capillary pressure decrease.

In the snap–off process, throats can be filled any where in the permeable medium and a connected wetting front is not needed. However, Piston like filling follows the same mechanism as drainage, and a well-connected wetting front is required. The capillary pressure required for snap off in a square throat is therefore

$$P_c = \frac{\sigma}{r}(\cos \theta - \sin \theta) \quad (2 - 2)$$

Not only this capillary pressure is smaller than the capillary pressure required for piston like filling as it shown in Eq. 2 – 1, but also, it takes time for water to move through the crevices to reach the throats. Therefore, depending on the layer flow velocity and capillary pressure either piston like filling or snap-off filling could be dominated. This can be explained by the CDC curve which is explained in the next section

2 – 2: Capillary Desaturation Curve

As we mentioned earlier, imbibition at the large scale is a combination of two pore scale mechanisms: piston like and snap- off. If piston like filling is the main mechanism in the displacement, as it shown in Fig. 1- 1 (a), all the pores and throat behind the main wetting front will fill with the wetting phase and saturation change will be abrupt. However, in the snap off dominated regime, wetting phase disperse through the whole permeable medium (Fig. 1 -1 (b)) and saturation change will be gradual. Whether the piston like or snap off filling is the controlling mechanism in the imbibition can be explained by the front velocity. In other words, at high frontal velocity water movement through the layer can not match the speed of front. Lenormand and Zarcone [1984], explained this behavior in terms of capillary number.

$$N_{Ca} = \frac{\mu v}{\sigma} \quad (2 - 3)$$

The capillary number is related to the ratio of the viscous forces (which scale as $v\mu$) to the capillary forces (which scale as σ) at the pore scale.

If capillary forces dominate the nonwetting phase will be trapped in disconnected blobs and ganglia through capillary forces. At high capillary numbers, the viscous drag creates

pressure drops that can disrupt the capillary interfaces, or more likely, prevent the interfaces from forming in the first place. The lack of interface will suppress snap off which results a diffuse front.

2 – 3: Pore Doublet Model

The other dimensionless number, which plays a role in the displacement processes, is Bond number. Same as capillary number, bond number is the ration of gravity to capillary forces.

$$N_{Bo} = \frac{\Delta\rho g L^2}{\sigma} \quad (2 - 4)$$

Where L is the characteristic length. In pore scale capillary, number and Bond number is in the order of 10^{-7} , 10^{-4} respectively.

Here, we use pore doublet model to capture the effect of bond number on residual oil saturation. Figure 2 – 6 shows a pore doublet model for imbibition process. As it shows in this figure, it is assumed when the wetting/ non-wetting interface reaches the out flow end of the doublet in either pass, the non- wetting fluid is trapped in the other path.

From the Poiseuille's equation, the volumetric flow rate in each path is given by the equation 2 – 4.

$$Q_i = \frac{\pi R_i^4}{8\mu l} (\Delta p_i + \rho g l), \quad i = 1, 2 \quad (2 - 5)$$

Since, the paths are parallel; the driving force across each path should be equal.

$$\Delta p_1 + \rho g l_1 - p_{c1} = \Delta p_2 + \rho g l_2 - p_{c2} \quad (2 - 6)$$

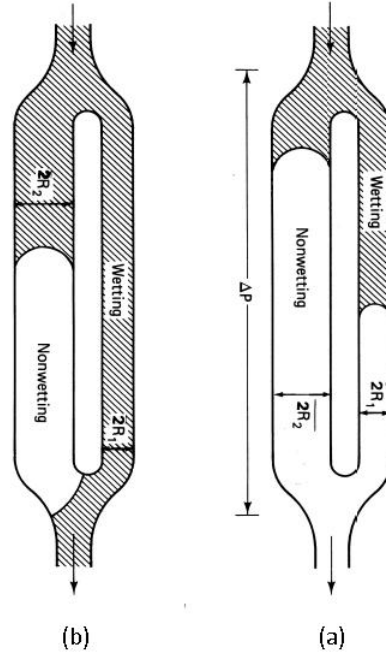


Figure 2 – 5 Schematic diagram of pore doublet model (a) before trapping, (b) after trapping
[Lake 1989]

From the Eq. 2 – 4 and 2 – 5 the total volumetric flow rate through the doublet is therefore

$$Q = \frac{\pi}{8\mu l} (R_1^4 \Delta p_1 + R_1^4 \rho g + R_2^4 (\Delta p_1 - p_{c1} + p_{c2}) + R_2^4 \rho g) \quad (2-7)$$

In Eq. 2 -6, the capillary pressures are positive for the imbibition process, however, in the drainage process the capillary pressures are negative. Therefore, as we show in the previous section, in the imbibition process non – wetting phase will be trapped in the large pores. However, in the drainage process, the wetting phase will be trapped in the small throats. Using these equations, we can write the volumetric flow in each path as a function of doublet geometry, and the interfacial tension.

$$Q = \frac{\pi R_1^4 \sigma \cos \theta}{8\mu l} \left(\frac{1}{R_2} - \frac{1}{R_1} \right) + \frac{\pi \Delta p_1}{8\mu l} (R_2^4 + R_1^4) + \frac{\pi \rho g}{8\mu l} (R_2^4 + R_1^4) \quad (2-8)$$

$$Q_1 = \frac{Q - \frac{\pi R_2^4 \sigma \cos \theta}{4\mu l} \left(\frac{1}{R_2} - \frac{1}{R_1} \right)}{1 + \left(\frac{R_2}{R_1} \right)^4} \quad (2-9)$$

$$Q_2 = \frac{\left(\frac{R_2}{R_1} \right)^4 Q + \frac{\pi R_2^4 \sigma \cos \theta}{4\mu l} \left(\frac{1}{R_2} - \frac{1}{R_1} \right)}{1 + \left(\frac{R_2}{R_1} \right)^4} \quad (2-10)$$

The amount of trapped non – wetting phase depends on the velocity at each path; the ratio of average velocity is therefore

$$\frac{Q_2 / \pi R_2^2}{Q_1 / \pi R_1^2} = \frac{v_2}{v_1} = \frac{\frac{\left(\frac{R_2}{R_1} \right)^4 Q + \frac{\pi R_2^4 \sigma \cos \theta}{4\mu l} \left(\frac{1}{R_2} - \frac{1}{R_1} \right)}{\pi R_2^2}}{\frac{Q - \frac{\pi R_2^4 \sigma \cos \theta}{4\mu l} \left(\frac{1}{R_2} - \frac{1}{R_1} \right)}{\pi R_1^2}} \quad (2-11)$$

Which is reduced to,

$$\frac{v_2}{v_1} = \frac{4 \left(\frac{R_1^4 \Delta P_1 + R_2^4 \Delta P_2}{8R_1^3 \sigma \cos \theta} \right) + \left(\frac{\rho g l (R_1^4 + R_2^4)}{8R_1^3 \sigma \cos \theta} \right) + \left(\frac{1}{\beta} - 1 \right)}{4 \left(\frac{R_1^4 \Delta P_1 + R_2^4 \Delta P_2}{8R_1^3 \sigma \cos \theta} \right) + \left(\frac{\rho g l (R_1^4 + R_2^4)}{8R_1^3 \sigma \cos \theta} \right) - \beta^2 \left(\frac{1}{\beta} - 1 \right)} \quad (2-12)$$

where $\beta = R_2/R_1$ is a heterogeneity factor [Lake, 1984], and

$$N_{cb} = \left(\frac{R_1^4 \Delta P_1 + R_2^4 \Delta P_2}{8R_1^3 \sigma \cos \theta} \right) + \left(\frac{\rho g l (R_1^4 + R_2^4)}{8R_1^3 \sigma \cos \theta} \right) \quad (2-13)$$

Where the first term is the capillary number $N_{ca} = \left(\frac{\mu Lv}{R\sigma \cos \theta} \right)$ and the second term is bond number $N_{bo} = \left(\frac{\rho g l R}{8\sigma \cos \theta} \right)$. Therefore, the amount of residual oil saturation is depending on both the capillary number and bond number.

2 – 4: Stability Analysis for a Sharp and Diffuse Front

The general theory of hydrodynamic stability addresses the question of whether a given fluid flow is stable relative to imposed disturbance. Here, we analyze the stability of the sharp and diffuse front

First assume we have sharp interface; stable front occurs when the interface between two fluids is flat and small perturbations of the interface decay over time. However, in unstable displacement, a perturbation can grow with time and stability depends on the density or viscosity difference of the displacing and displaced fluid.

A linear stability analysis for sharp front is performed on the Saffman – Taylor problem in order to get the instability. We use the perturbation theory with a plane wave solution that corresponds to the state of stability analysis.

Consider an immiscible displacement of phase 2 by phase 1 in the vertical direction where Z-axis is positive downward as it shown in Fig. 2 - 7. The flow rate in region 1 is equal to Eq. 2 – 11

$$Q_1 = -\frac{kk_{r1}}{\mu_1} \nabla(p_1 - \rho_1 gz) \quad (2 - 14)$$

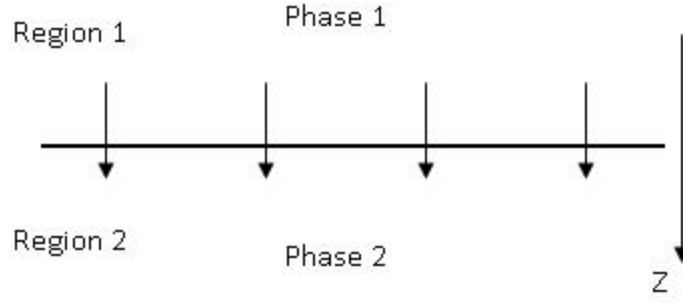


Figure 2-6 Schematic diagram of vertical displacement of phase 2 by phase 1

We define the average velocity as Eq. 2 – 12, which is equal to

$$v = \frac{Q}{\phi S} = -\frac{kk_r}{\phi\mu_1 S} \nabla(p - \rho gz) \quad (2 - 15)$$

At time $t = 0$, region 1 is only consist of phase 1 ($S_1 = 1, S_2 = 0$), and region 2 is only consist of phase 2 ($S_1 = 0, S_2 = 1$). Therefore, the average velocity of phase 1 in region 1 and phase 2 in region 2 is equal to

$$v_1 = -\frac{k}{\phi\mu_1} \nabla(p_1 - \rho_1 gz) \quad (2 - 16)$$

$$v_2 = -\frac{k}{\phi\mu_2} \nabla(p_2 - \rho_2 gz) \quad (2 - 17)$$

We define the gravity potential as

$$v_1 = \nabla\lambda_1 \Rightarrow \lambda_1 = -\frac{k}{\phi\mu_1} (p_1 - \rho_1 gz) \quad (2 - 18)$$

$$v_2 = \nabla\lambda_2 \Rightarrow \lambda_2 = -\frac{k}{\phi\mu_2} (p_2 - \rho_2 gz) \quad (2 - 19)$$

In each region $\frac{\partial q_i}{\partial s} = 0$, therefore, by using conservation of mass in each region

$$\frac{\partial s_1}{\partial t} = 0 \Rightarrow \nabla \cdot v_1 = 0, \nabla^2 \lambda_1 = 0 \quad (2-20)$$

$$\frac{\partial s_2}{\partial t} = 0 \Rightarrow \nabla \cdot v_2 = 0, \nabla^2 \lambda_2 = 0 \quad (2-21)$$

Now, we perturb the front as it is shown in Fig. 2 - 8, if the perturbation grows with time the front will be unstable, otherwise it will be stable.

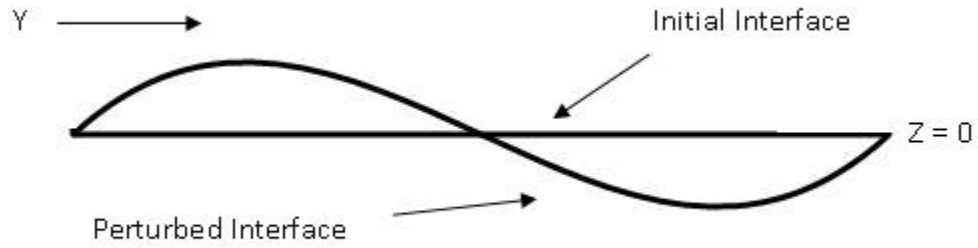


Figure 2 – 7 Perturbed interface, it can happen in the real medium because of the micro heterogeneity

Assume that the interface is initially at $z=0$ and the perturbed interface is formulated as

$$\zeta = ae^{in_y \cdot y + \omega t} \quad (2-22)$$

Therefore, if $\omega > 0$, the perturbation increases with time and because of that it is unstable.

However, if $\omega < 0$, perturbation decreases with time and it is stable. We can calculate the front velocity as follow.

$$\frac{\partial \lambda_1}{\partial z} = v_{1z} = U + \frac{\partial \zeta}{\partial t} \quad (2-23)$$

Fluid potential can be calculated by integrating the Eq. 2 -20

$$\lambda_1 = U_z + a\omega e^{in_y \cdot y + \omega t} f(z) + g(y) + C_1 \quad (2-24)$$

Here, we use Laplace equation to find the unknown functions $f(z)$, $g(y)$, which yields to,

$$\lambda_1 = U_z + \frac{a\omega}{n_y} e^{in_y y + \omega t + n_y z} + C_1 \quad (2-25)$$

$$\lambda_2 = U_z - \frac{a\omega}{n_y} e^{in_y y + \omega t - n_y z} + C_2 \quad (2-26)$$

Now, at the boundary $P_e = P_2 - P_1$ @ $z = \zeta$, and if phase 1 is the wetting phase $P_e < 0$,

from the equation 2-3 and 2-4, we can derive P as a function of λ as follow,

$$p_1(z = \zeta) = -\frac{\mu_1 \phi}{k} \zeta \left(U + \frac{\omega}{n_y} \right) + \rho_1 g \zeta - \frac{\mu_1 \phi}{k} C_1 \quad (2-27)$$

$$p_2(z = \zeta) = -\frac{\mu_2 \phi}{k} \zeta \left(U + \frac{\omega}{n_y} \right) + \rho_2 g \zeta - \frac{\mu_2 \phi}{k} C_2 \quad (2-28)$$

From that, the angular frequency (ω) can be calculated as

$$\omega = \frac{n_y k}{\phi(\mu_1 + \mu_2)} \left[(\rho_1 - \rho_2) g - \frac{(\mu_1 - \mu_2) \phi}{k} U \right] \quad (2-29)$$

As mentioned earlier if $\omega > 0$, the perturbation is unstable.

$$\left[(\rho_1 - \rho_2) g - \frac{(\mu_1 - \mu_2) \phi}{k} U \right] > 0 \quad (2-30)$$

And perturbation is stable if

$$\left[(\rho_1 - \rho_2) g - \frac{(\mu_1 - \mu_2) \phi}{k} U \right] < 0 \quad (2-31)$$

From the equation 2-27 and 2-28 the Saffman – Taylor instability for the sharp front is summarized in Table 2-1

For diffuse front, a travelling wave solution of one dimensional Richard's equation is used for basic flow equation [Du et al., 2001],

$$\phi \frac{\partial s}{\partial t} = \frac{\partial}{\partial z} \left(D(s) \frac{\partial s}{\partial z} - K(s) \right) \quad (2-32)$$

Where D and K are diffusivity and conductivity respectively. Travelling wave solution has the following form

$$\eta = z - vt \tag{2 - 33}$$

Where

$$v = \frac{K(s) - K(s_0)}{S - S_0} \tag{2 - 34}$$

A standard perturbation technique can be applied

$$s = s(z, t) + \varepsilon v(z, t) \tag{2 - 35}$$

The physics behind the stability analysis for the diffuse front is complicated to be discussed in our module. However, the results show that the diffuse front is always stable. [Chuoque *et al.*, 1959; Parlange and Hill, 1976; Glass *et al.*, 1991; Wang *et al.*, 1998; Du *et al.*, 2001]

Table 2 - 1 Saffman – Taylor instability criteria for sharp front [Saffman and Taylor, 1958].

	$\mu_1 > \mu_2$	$\mu_1 < \mu_2$
$\rho_1 > \rho_2$	Low Velocities: Unstable High Velocities: Stable	Always Unstable
$\rho_1 < \rho_2$	Always Stable	Low Velocities: Stable High Velocities: Unstable

2 – 5: Preferential Flow and Saturation Overshoot

Preferential flow refers to the uneven and rapid movement of displacing fluid through the permeable medium. Preferential flow describes three different processes. Macro pore, funnel flow, and finger flow. In macro pore, displacing fluid passes through the high

permeability routes caused by roots and worms. Funnel flow is referred to as a preferred path of displacing fluid due to impermeable layer.



Figure 2 – 8 Formation of soil water fingers. Photo was taken in Port Campbell National Park, 60 km east of Warrnambool, Australia. [Stagnitti et al., 1998]

Unlike the other two processes which happen in the heterogeneous medium, finger flow happens in the homogeneous medium (as it shown in Fig. 2 – 9); where the displacing fluid flows through the preferred path. Finger flow refers to instability of the interface when a higher density fluid (e.g. water) displaces a lower density fluid (e.g. air) at low velocities (Table 2 – 1). Depending on the displacement direction, it has been called gravity – driven fingering or viscous fingering. As shown in the previous section, when a dense viscous fluid invades in to a less dense, less viscous fluid at a low flow rate the front is predicted to be unstable. However, experimental investigations show that at a very low flow rate (~ 0.01 ml / min), displacement becomes stable again. Therefore, it still remains unclear, when infiltration is likely to be unstable and produce preferential flow, or stable and laterally uniform.

Experimental observations have shown that gravity driven fingering exhibit saturation overshoot, with high saturation behind the front (thereafter called tip) followed by the lower saturation behind the tip (thereafter called tail). The schematic diagram of preferential flow is shown in figure 2 – 10. From these observations, it has been proposed that saturation overshoot is a necessary and sufficient prerequisite for gravity-driven fingering, i.e., gravity-driven fingering will occur if and only if saturation overshoot occur. Saturation overshoot is a result of a sharp front [Geiger and Durnford, 2000; Eliassi and Glass, 2001].

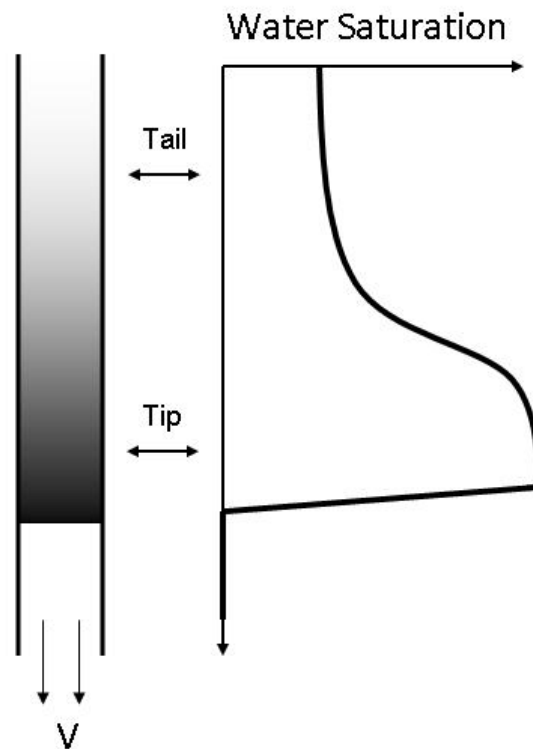


Figure 2 – 9 Schematic of a sharp front and the associated water saturation within the flow path. Saturation over shoot occurs when the tip saturation is greater than the tail saturation.

Previous studies [Glass *et al.*, 1989; Selker *et al.*, 1992; Liu *et al.*, 1994; DiCarlo, 2004; Rezanezhad *et al.*, 2006] have shown that saturation overshoot occurs in a certain medium when the applied flux is below the saturated hydraulic conductivity, as what we

expect from the stability analysis. However, at low flux saturation profile is uniform with no saturation overshoot. If the medium has initial water, saturation overshoot is either repressed or does not occur at all [*Bauters et al.*, 2000; *Diment and Watson*, 1985]. Importantly, infiltration studies have also shown that below a certain flux (hereafter called the overshoot flux) saturation overshoot ceases [*DiCarlo*, 2004; *Yao and Hendrickx*, 1996]. With no saturation overshoot, the infiltration follows a standard unsaturated flow model with saturation increasing monotonically from the initial condition to the final condition. Simply, saturation overshoot occurs when, for some reason, the pore filling mechanisms cause too many pores to be filled, achieving an excess saturation, at the initial wetting front [*DiCarlo*, 2004; 2006].

We hypothesize that different pore filling mechanisms dominate below and above the overshoot flux. At low frontal velocities, the wetting phase has time to establish and move through wetting layers ahead of the main wetting front. This provides the wetting phase access to pores at a large distance ahead of the main wetting front, and then capillary forces determine which of these pores will fill. The sizable layers allow both snap-off filling mechanisms (where the wetting phase fills a pore or throat from the swelling of the layers) ahead of the front, and piston-like invasion percolation mechanisms at the front [*Blunt and Scher*, 1995]. As there is a range of pore and throat sizes and available filling mechanisms, this leads to a spatially diffuse front, and on a macro-scale, a relatively smooth increase of the saturation at the front. With this smooth increase, saturation overshoot does not occur and continuum based models are appropriate to describe the infiltration behavior.

In contrast, as the speed of the wetting front increases, the formation of wetting layers and wetting phase flow through these layers is suppressed relative to flow at the main

wetting front. Not only is the spatial range of available pores and throats lessened, the thinner or absent layers greatly suppress the snap-off filling mechanism. This leaves only the piston-like invasion percolation filling mechanism at the main wetting front. But since this mechanism is collective, i.e. if one pore fills, it makes it more likely for its neighbor to fill, this can cause overfilling of the pores, and in turn saturation overshoot. This suppression of snap-off will occur if the front is sharp at the pore scale. This is roughly the same mechanism which has been proposed to explain the capillary desaturation curve, where the residual non-wetting fluid is lowered with increasing capillary number due to the suppression of snap-off.

In this work, we use overshoot to study the dynamics at the initial wetting front as a function of imbibing fluid properties. We perform overshoot measurements as a function of flux for six different non aqueous liquids, three alkanes (hexane, octane, and decane) and three alcohols (methanol, ethanol, and propanol). These liquids give us a range of molecular weights, viscosities, vapor pressures, and miscibility with the initial adsorbed water on the grain surfaces.

2 – 6: Sharp and Diffuse Front

In the micromodel experiments described by the Lenormand and Zarcone, two types of wetting fronts are identified: a flat frontal advance regime (Fig 2 – 11 a) and a bond percolation regime (Fig 2 – 11 c). In the flat frontal advance regime, the displacing fluid occupies nearly all the pores and throats behind the main wetting front and the saturation changes abruptly in space (sharp front). In the bond percolation regime, pores are filled gradually at the main wetting front, and the saturation change is gradual in space (diffuse front). Diffuse front is seen for a low capillary number and contact angle when the snap-

off is dominant. At high frontal velocity snap – off filling can not match the speed of bulk, therefore, the piston like filling is dominant, however at low a flow rate where the capillary force is dominant, this flow regime is more probable. The end point relative permeability of water (Fig. 2 – 11c) is 0.15 [Hughes, 1998]. Despite the fact that, the typical relative permeability for water flooding in strong water wet medium is around 0.5.

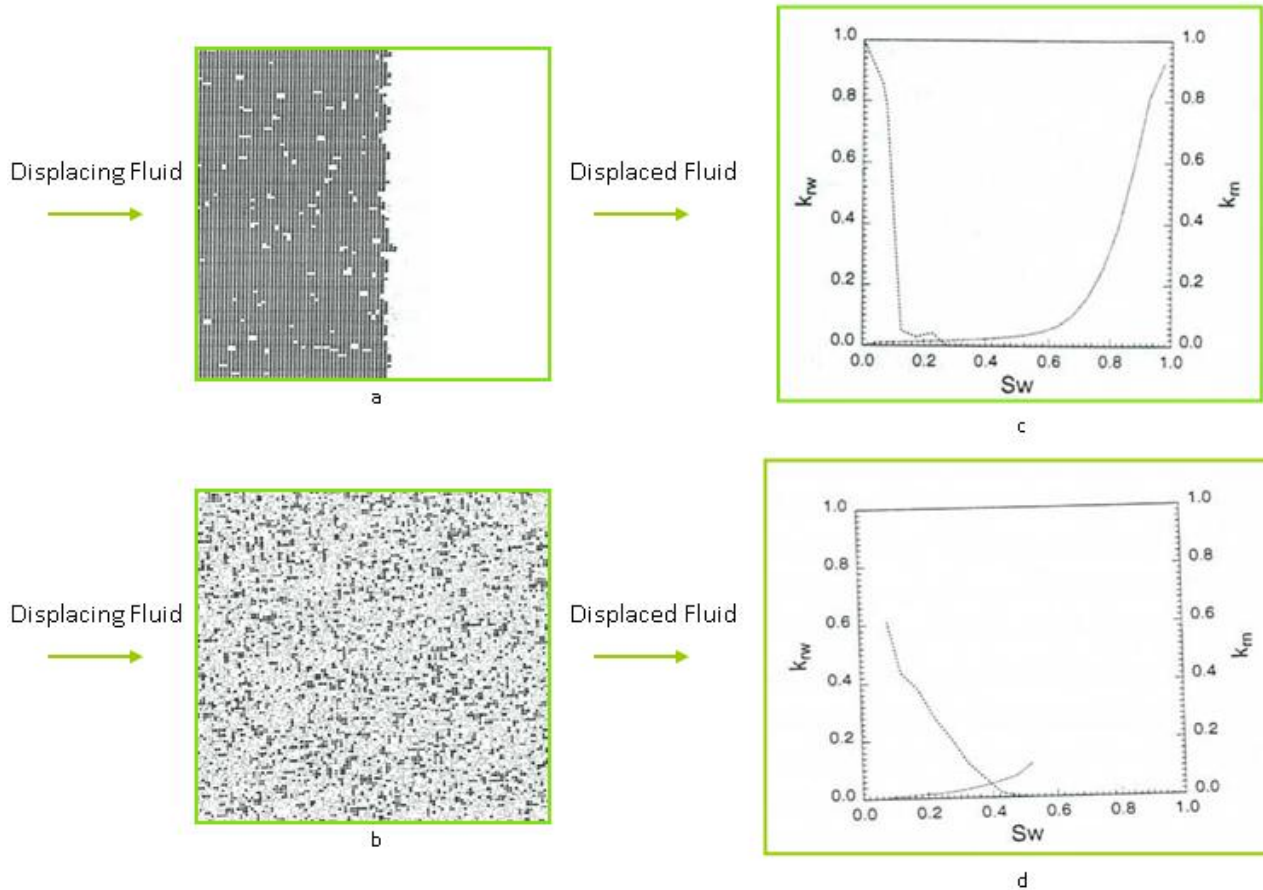


Figure 2 – 10 Network model sharp and diffuse front and the corresponding relative permeability curves. [Hughes and Blunt 2001]

Sharp fronts occur at a high capillary number with very low initial wetting phase saturation. This regime is completely the opposite of the diffuse front in pore filling mechanism. In sharp front, piston like filling is dominates and the snap – off filling can not match the speed of front. Therefore, only a small part of the pores and throats are by pass, resulting in a small residual saturation. In this regime saturation changes from $S_w =$

1 - S_{or} to S_{wi} over a one or two grain size. Figure 2 – 11 b shows that the relative permeability of the flat frontal advanced. However, only the end points have a physical meaning as the rest of the saturations are jumped over.

Chapter 3: Materials and Methods

Sharp and diffuse fronts are observed in 2D macro model of Lenormand and Zarcone [1984]. This behavior is also observed in the 2 and 3D network models of Hughes and Blunt [2001]. To observe the behavior in the real medium we conduct a vertical infiltration experiment in the slim tube with diameter less than a finger width (finger size is observed to depend on the grain size). We observe that at low flux the saturation profile is uniform and front is diffuse (as observed in macro model and network model), by increasing the flow rate, saturation at the front exceed the saturation behind the front and saturation change will be abrupt in space (as observed in the sharp front). Therefore, by measuring the flux at which the saturation overshoot ceases and understanding the physics behind that, we can find the transition between sharp and diffuse front.

Four different sands (mined in Ottawa, Minnesota, Unimin Corporation) were used as the permeable medium in different experiments. The sand has smooth and almost spherical grains (Fig. 3 – 1) , and its flow characteristics and the van Genuchten [*van Genuchten*, 1980] fitting parameters to the pressure – saturation curve are listed in Table 3 - 1 [*DiCarlo*, 2004]. The sand was washed with distilled water and subsequently dried before use.

The vertical infiltration experiments were carried out with the sand packed into a 0.5 m long and 0.95×10^{-2} m diameter tube; the tube diameter is small enough to keep the flow uniform laterally, but large enough to avoid finite size effects (i.e. much greater than the grain size).



Figure 3 – 1 Photograph of the spherical grains of the 12/20 sand. [DiCarlo 2004]

A one holed rubber stopper and a screen were placed in the bottom to keep the sand in the tube while permitting air flow out from the bottom. The experimental tube was dry packed using an extension tube with two randomizer screens to produce a uniform pack. Three different alcohols and alkanes were used as infiltration fluids, adding to previous measurements with water as an infiltrating fluid [DiCarlo, 2004]. The fluid properties are listed in Table 3 - 2.

Table 3 -1 Physical parameters for the four sands used in the study [Schroth et al.]

Sand	d ₅₀ (m)	K (m ²)	φ	s _r	Drainage		Imbibition	
					α, (m ⁻¹)	n	α, (m ⁻¹)	N
12/20	1.105 x 10 ⁻³	5 x 10 ⁻¹⁰	0.35	0.034	12.9	9.70	30.3	4.98
20/30	0.713 x 10 ⁻³	2.5 x 10 ⁻¹⁰	0.35	0.045	9.95	10.57	17.7	6.23
30/40	0.532 x 10 ⁻³	1.5 x 10 ⁻¹⁰	0.35	0.051	6.7	13.1	17.3	10.0
50/70	0.261 x 10 ⁻³	0.52 x 10 ⁻¹⁰	0.35	n/a	n/a	n/a	n/a	n/a

A light transmission method (LTM) was used to measure the saturation profile within the sand column as a function of space and time [Selker et al., 1992]. The light transmission system was composed of a stable and low temperature light box, a black plywood mask,

and a light detector. The light box consists of a (1.06 x 0.35 m) box with four vertical fluorescent lamps to apply uniform output light. The black plywood mask had three identical vertical slits (0.55 x 0.006 m) on which the tubes were secured vertically. The center tube was saturated completely with the experimental fluid and provided an intensity reference for each image. On each side of the center tube identical experimental tubes were run in duplicate. The light detector, a Canon Rebel Xti camera, was placed 1.15 m in front of the chamber; and pictures were taken at regular time intervals. The camera had a spatial resolution of 2816x1880 pixels. The exposure time varied between 0.3 to 0.8 s depending on the infiltration rate, and focal length of 45×10^{-3} m was used in every experiment. Schematic diagram of apparatus is shown in Fig. 3 – 2.

Table 2: Physical properties of fluids

	Density	Vapor Pressure	Surface Tension	Viscosity
	Kg / m ³	KPa	N/m	Pa. s
Water	997.0	3.13	71.97×10^{-3}	0.898×10^{-3}
Methanol	796.4	16.96	29.59×10^{-3}	0.545×10^{-3}
Ethanol	796.6	7.80	22.10×10^{-3}	0.962×10^{-3}
Propanol	793.9	2.83	26.31×10^{-3}	1.9×10^{-3}
Hexane	666.3	20.22	17.86×10^{-3}	0.298×10^{-3}
Octane	708.3	1.95	22.35×10^{-3}	0.515×10^{-3}
Decane	735.1	0.21	23.07×10^{-3}	0.846×10^{-3}

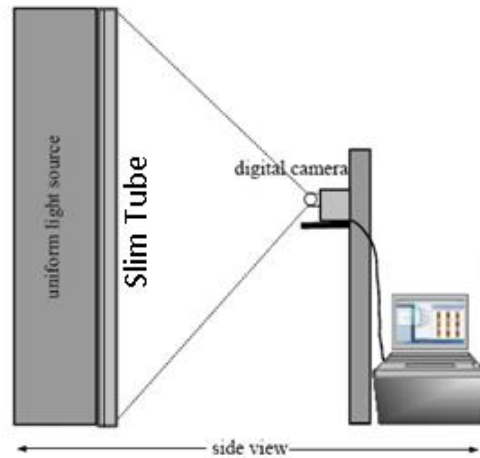


Figure 3 -2 Schematic diagram of apparatus used in this study.

The infiltrating fluid was applied at the top of the column through a B-D needle (19G1) and the flux was held constant with a KD Scientific (RS232) syringe pump. The pump provided fluid injection rates from 1.6×10^{-11} to 1.6×10^{-7} m³/s. The injection process continued until the injecting fluid reached the bottom of the column. More than 30 experiments were performed as a function of flux for each fluid. In-situ fluid saturation during the infiltration can be calculated using the light transmission data through two different techniques.

As light propagates through a homogeneous medium, it is absorbed exponentially in accordance with Beer's law (Eq. 3 – 1). For a specific wavelength of light, the measured radiant flux (herein referred to as intensity), I , transmitted through a medium of thickness d is given by

$$I = CI_0 \exp(-\alpha d) \tag{3 – 1}$$

where I_0 is the measured intensity of the light and α_i is the absorption coefficient. Since the intensity of diffuse light drops approximately with the square of distance, and the

distances from the detector to the medium and the source are not necessarily the same, C is an optical geometric term that corrects for differences between points of emission and observation. For collimated light, or if the source and medium are approximately the same distance from the detector, C can be omitted. It is important to note that α is strongly wavelength-dependent, given that most translucent medium is a color other than neutral gray. [Niemet and Selker, 2001]

A homogeneous permeable medium of uniform liquid content can be considered as a single phase, with an effective Beer's law absorption coefficient representative of the bulk medium. However, at the pore scale, light passes through solid, liquid, and gas phase constituents, each with a separate absorption coefficient. We use this method to measure the intensity in the light transmission [DiCarlo, 2004; Glass *et al.*, 1989; Niemet and Selker, 2001; Rezanezhad *et al.*, 2006] The light intensity of every pixel was taken from the images using MATLAB and averaged over 0.1×10^{-2} m horizontally and 0.29×10^{-2} m vertically. The intensity of light was normalized by comparing to the light intensity of fully saturated column,

$$I_n(z,t) = \frac{I(z,t) - I(z,0)}{I_s(z,t) - I_s(z,0)} \quad (3 - 2)$$

where $I(z,t)$ is the intensity of the infiltration column with $I(z,0)$ being the intensity of the dry column, and $I_s(z,t)$ is the intensity of the fully saturated column. The saturation was obtained by assuming the saturation is linear with the normalized intensity [Tidwell and Glass, 1994; Niemet and Selker, 2001], and the proportionality constant is obtained using conservation of mass [DiCarlo 2004]. This is the saturation that is reported in the following results.

Chapter 4: Results and discussion

As mentioned in the introduction, we hypothesize that saturation overshoot is controlled by the pore filling mechanism. This behavior can be explained qualitatively by the capillary desaturation curve (CDC), at high fluxes the viscous forces are dominant, the pore filling is more likely piston-like, and saturation overshoot observed. However, at low fluxes capillary pressure is dominant and the displacement takes place by snap off filling, therefore the front is stable and no saturation overshoot occurs. To validate our hypothesis, constant infiltration in homogenous one dimensional permeable medium has been conducted with different fluids and grain sizes over large range of injection rates. The saturation profile was measured using light transmission method to observe whether the saturation overshoot occurs.

In this chapter, first we analyze the different experimental results followed by the mathematical model to describe the saturation overshoot. Finally, we will discuss the results as a function of fluid and medium properties.

4 – 1: Experimental Results

Figure 4 – 1 shows the snap shot of ethanol saturation as a function of vertical distance at four different fluxes for 30 /40 sand. As shown in Fig. 4 – 1, at low flux (2.3×10^{-6} m/s) the saturation profile is monotonic and no saturation overshoot occurs, but by increasing the flow rate saturation at the front increases more rapidly than the saturation behind the front and saturation overshoot occurs. Slight oscillations in saturation profile are noise from the granularity of the medium that occurs due to light transmission technique.

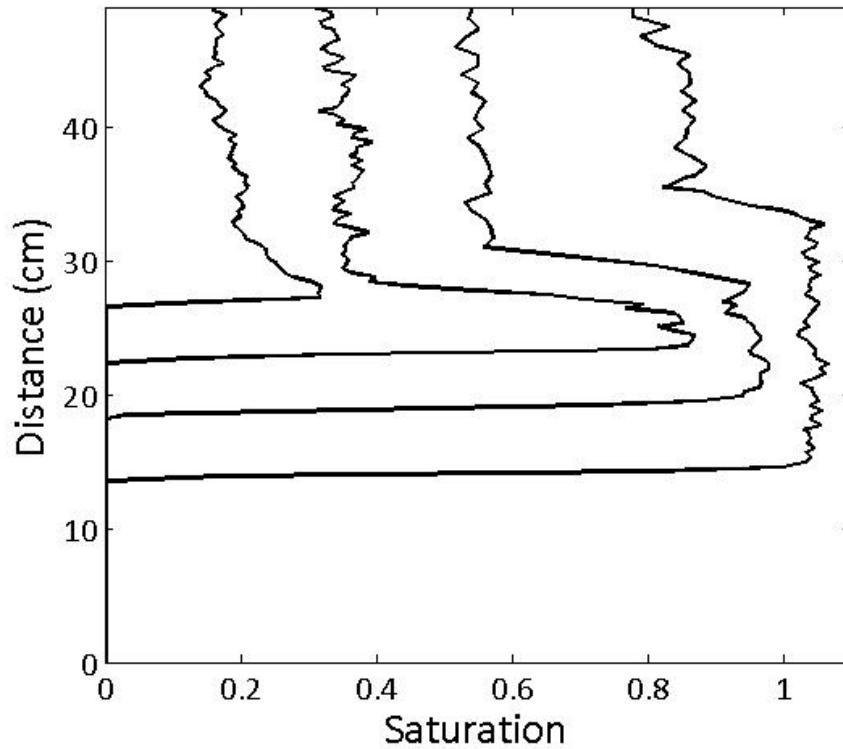


Figure 4 – 1 Snapshots of the ethanol saturation profile versus depth for four different applied fluxes. From top to bottom fluxes are 5.83×10^{-4} m/s, 2.33×10^{-4} m/s, 4.66×10^{-5} m/s and the lowest flux is 2.33×10^{-6} m/s. The tip and tail saturation decrease when the injected flux is decreased.

Figure 4 – 2 shows the measured tip and tail saturation as a function of injected flux for ethanol as the infiltrating fluid. The tip saturation was obtained by averaging the saturation $1.5 \times 10^{-2} - 3.5 \times 10^{-2}$ (m) behind the front, and the tail saturation was averaged over the saturation 0.15 - 0.17 m behind the front, (when the tip length is less than 0.15 m); scatter in the data from the multiple experiments gives an estimate of accuracy and repeatability. The fluxes for which the overshoot is observed (the overshoot region) are clearly recognizable, as this is where the tip saturation exceeds the tail saturation. Since the saturation becomes constant in the tail, the tail saturation S_{tail} is the saturation that balances the viscous and gravitational forces through the Darcy -Buckingham equation,

$$q = \frac{kk_r(S_{tail})\rho g}{\mu} \quad (4-1)$$

where q is the applied flux, k is the permeability, k_r is the relative permeability, g is the gravitational constant, ρ is the fluid's density, and μ is its viscosity. In soil physics nomenclature, the right hand side is simply the unsaturated conductivity of the medium when the invading fluid is water [DiCarlo, 2004].

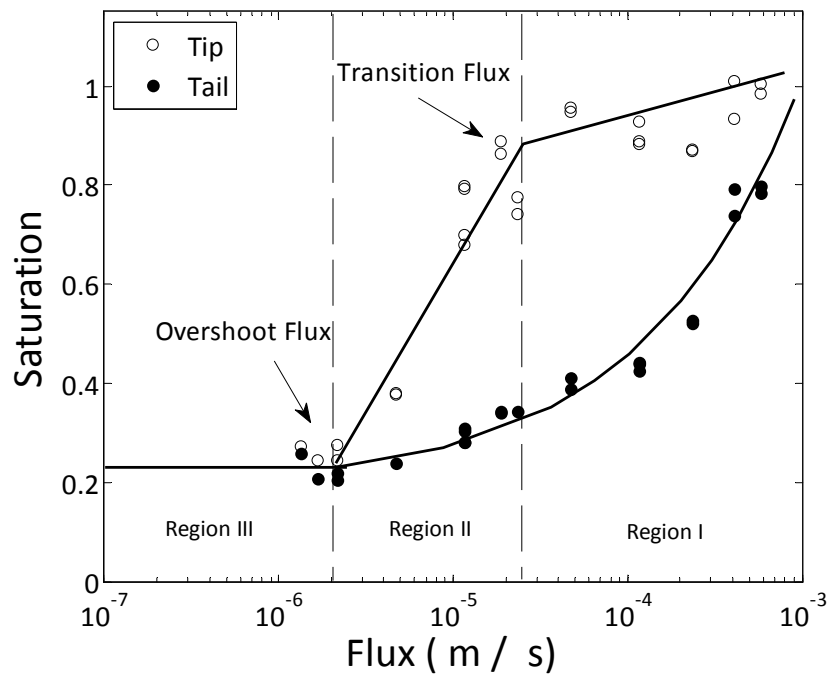


Figure 4 -2 Measured tip and tail saturation as a function of flux for ethanol. Three regions can be identified. The overshoot flux marks the onset of overshoot, and is equal to 2.05×10^{-6} m/s.

Here, we concentrate on the tip saturation, since this is what determines whether or not there is overshoot. Three saturation regions are identified in Fig. 4 – 2 as a function of flux.

Going from high flux to low flux, we start at the flux corresponding to the permeability of the medium (table 1) under the gravitational gradient of the applied fluid. Here the tip and the tail are both completely saturated. With decreasing flux, the tip saturation

decreases only slightly, while the tail saturation decreases greatly. Thus in this region (Region I) these fluxes exhibit saturation overshoot. Eventually the tip saturation begins to decrease rapidly below a certain flux. We label this flux as the transition flux; it is the transition between Region I and Region II or in other words at the transition flux the severe saturation overshoot occurs (the difference between saturation tip and tail is maximum).

In Region II, the tip saturation eventually meets the tail saturation at a much smaller flux. We label this flux the overshoot flux as this is the minimum flux for overshoot. Below the overshoot flux, infiltrations are in Region III with no overshoot. These two fluxes are evident for all permeable medium, initial conditions, and fluid pairs which exhibit overshoot. For initial conditions and media properties which show no overshoot, we can assume, without loss of generality, that the overshoot flux is greater than the largest applied flux (the saturated conductivity). This situation occurs for water infiltrations into pre-wetted sands [DiCarlo, 2004], and media with wider pore size distributions.

Determining whether or not saturation overshoot occurs at a certain flux is difficult to determine through experiments on or near the overshoot flux. Instead, as shown in Fig. 4 – 2, we fit the tip saturation in each of the three regions with a straight line on the semi log plot. The actual functional form may not be piecewise, as is shown, the fit is done only to have a standard way of finding the transition and overshoot fluxes because of the scatter in the data and lack of overriding theory. Using this method, the overshoot flux is determined by the intersection of the fitted tip and tail saturations. In the following section we explore the overshoot and transition flux as a function of fluid type and fluid properties.

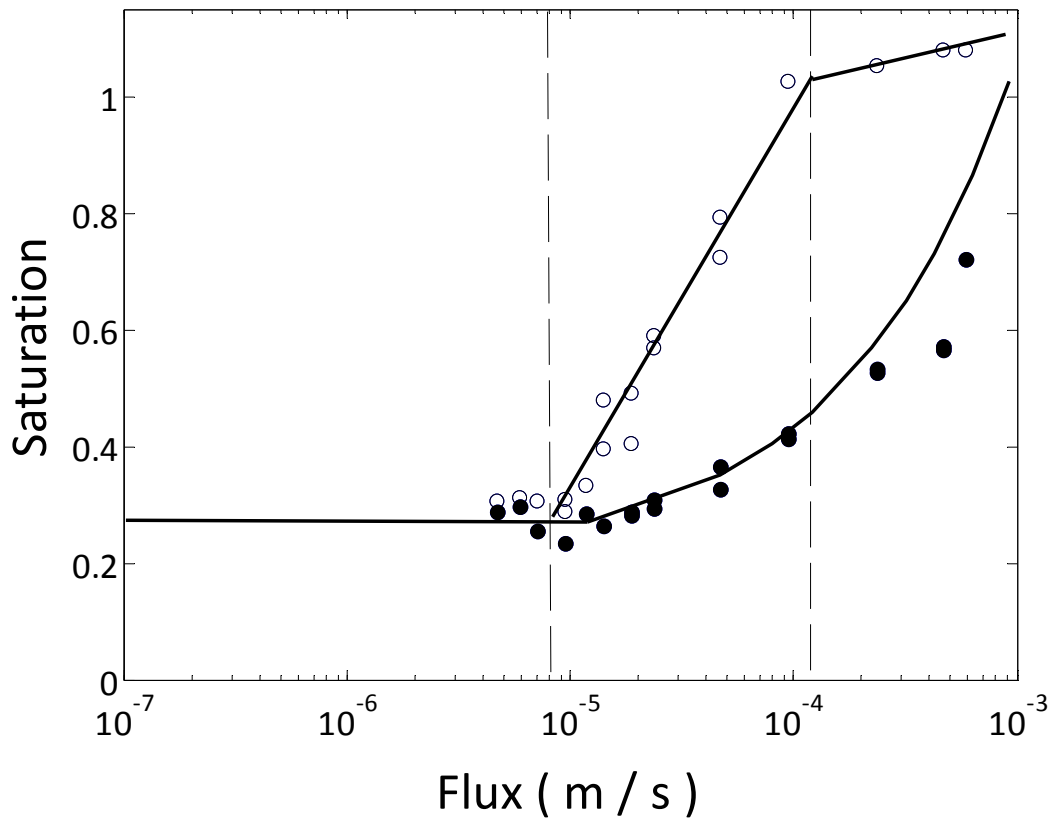


Figure 4 – 3 Measured tip and tail saturation as a function of flux for methanol. Methanol has an overshoot flux of $8.33 \times 10^{-6} \text{ m / s}$.

Figure 4 – 3 plots the tip and tail saturation for methanol as a function of infiltration flux. The pattern and regions are similar to Fig. 4– 2, only with a larger overshoot flux and a larger transition flux. Figure 4 – 4 shows the tip and tail saturation as a function of flux for propanol.

Again, these data are similar to Fig. 4 – 3, only with smaller overshoot flux. Together, Figs. 4– 2, 4– 3, and 4 – 4 show that the overshoot flux for alcohols decreases with the increasing amount of carbon atoms in the alcohol (increasing in molecular weight).

Figures 4 – 5, 4 – 6, and 4 – 7 show plots of tip and tail saturation for hexane, octane, and decane versus infiltration flux. Again these figures all show the same pattern of an overshoot flux and a transition flux. Like alcohols, the overshoot flux and transition flux

for alkenes decreases with increasing amount of carbon atoms in alkanes (increase in molecular weight).

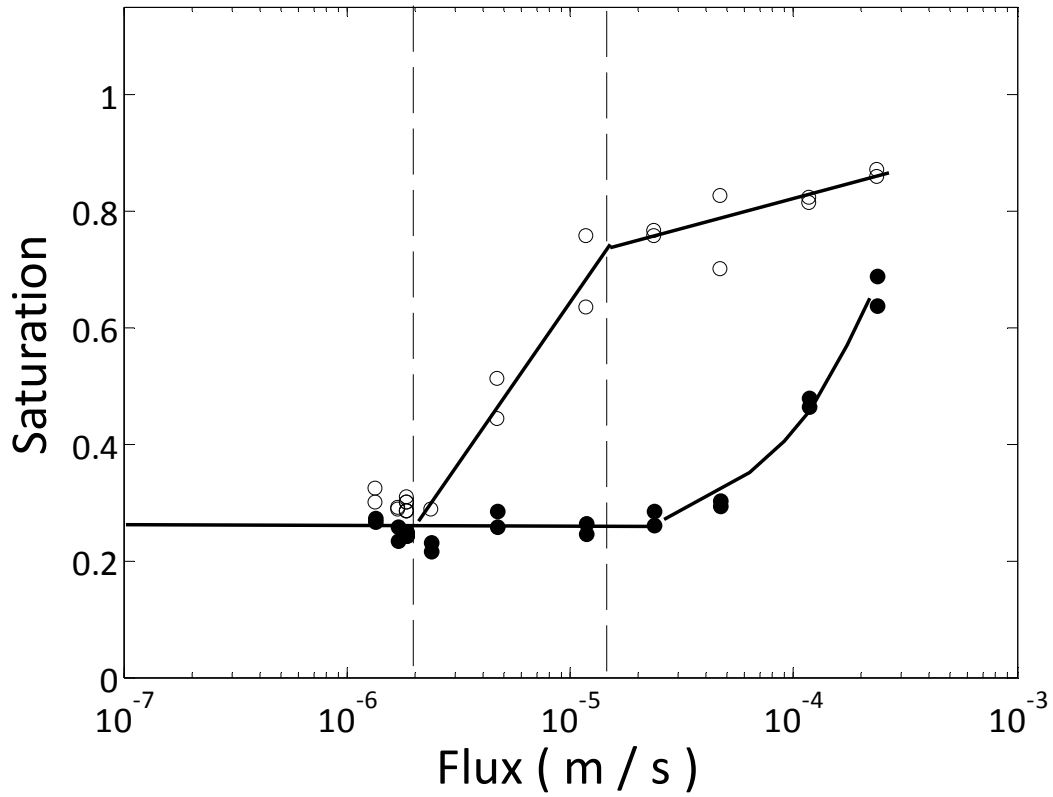


Figure 4 – 4 Measured tip and tail saturation as a function of flux for iso – propanol. Iso – propanol has an overshoot flux of 1.96×10^{-6} m / s.

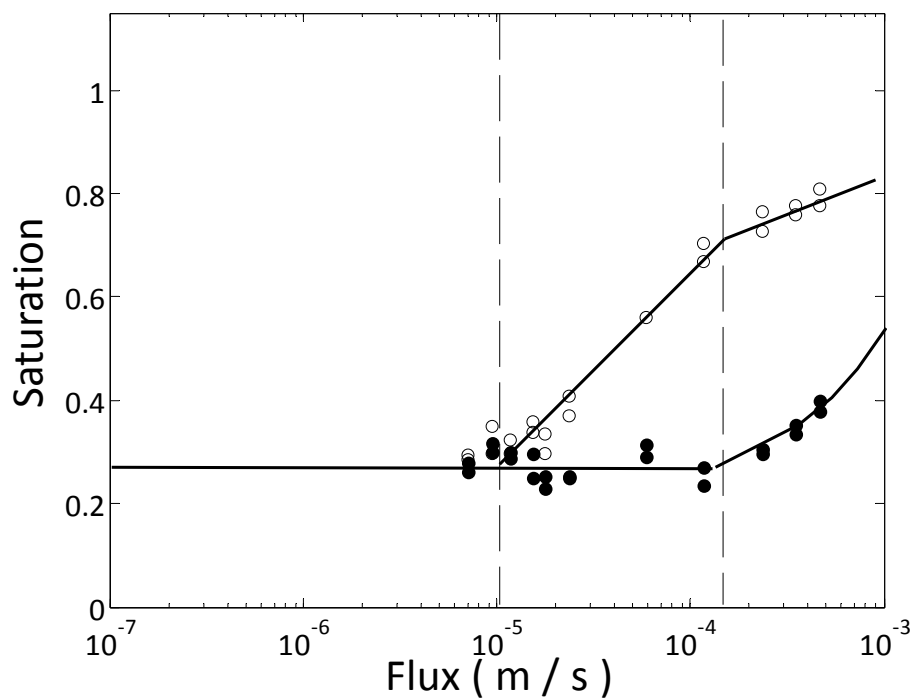


Figure 4 – 5 Measured tip and tail saturation as a function of flux for hexane. Hexane has an overshoot flux of 1.13×10^{-5} m / s.

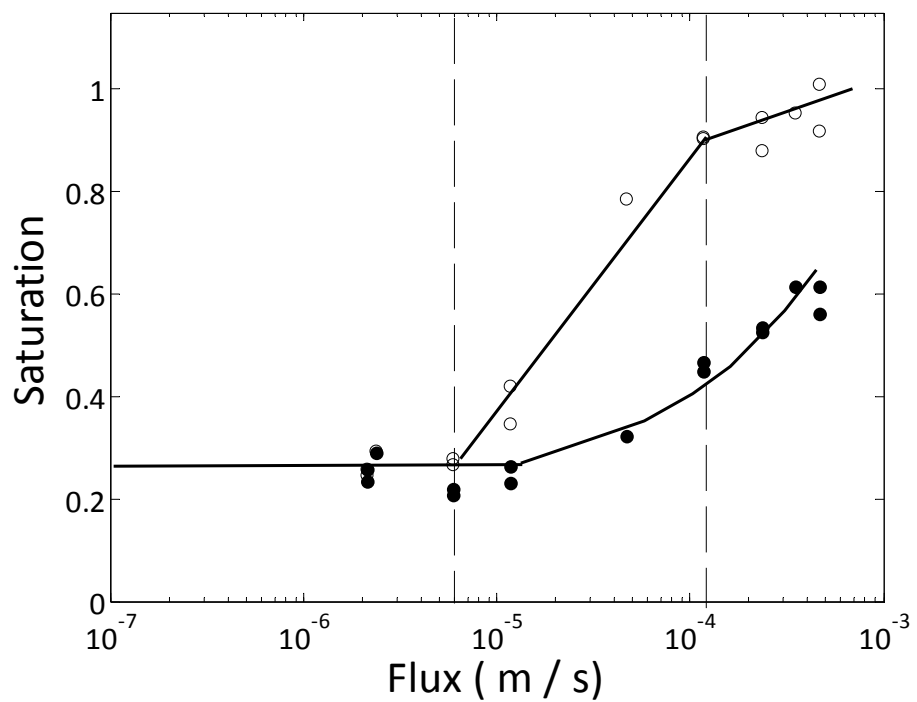


Figure 4 – 6 Measured tip and tail saturation as a function of flux for octane. Octane has an overshoot flux of 6.16×10^{-6} m / s.

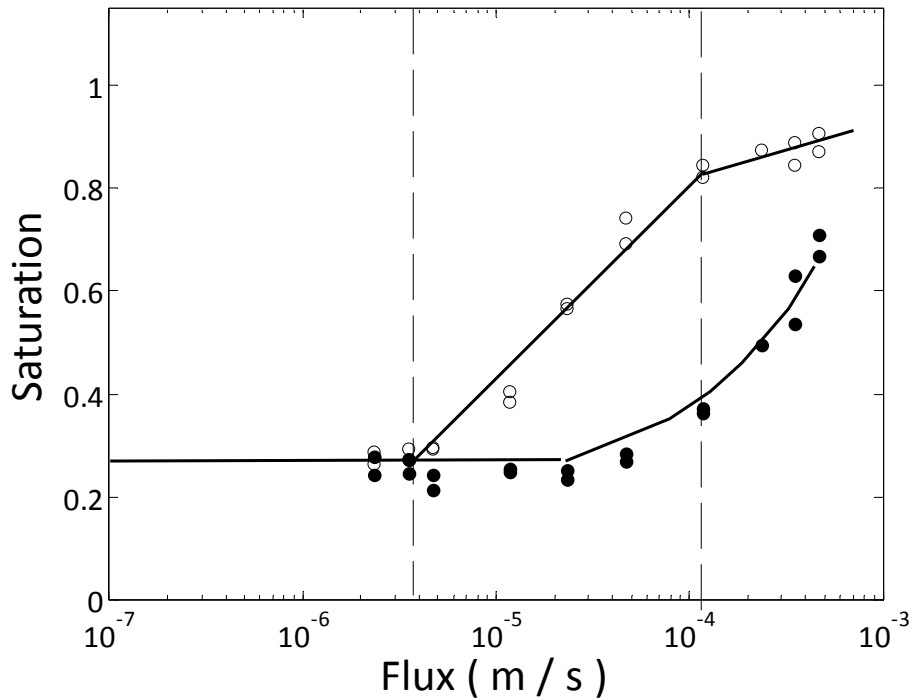


Figure 4 – 7 Measured tip and tail saturation as a function of flux for decane. Decane has an overshoot flux of 3.68×10^{-6} m / s.

In addition to the tip and tail saturations versus flux, we measured the tip length corresponding to the overshoot.

Next, we measured the overshoot flux as a function of media properties. Same experiments were conducted with different grain size. Figure 4 - 8 plots the measured tip and tail saturation as a function of flux for the same dry 30/40 sand. Again, the region where saturation overshoot is present is clearly demarcated where the tip saturation exceeds the tail saturation. In this case, the overshoot flux is calculated from the method explained earlier to be 2.13×10^{-6} [DiCarlo 2004].

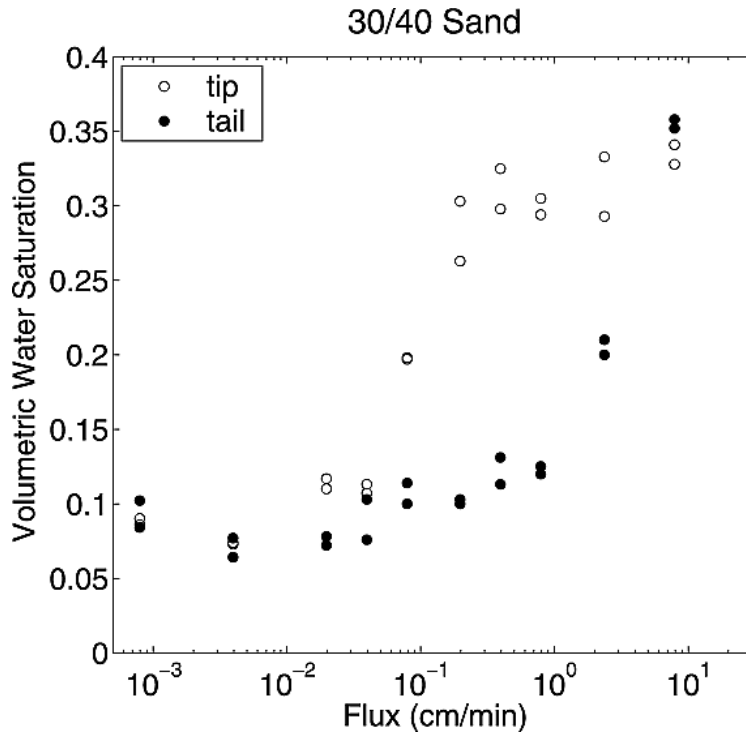


Figure 4 – 8 Measured tip and tail saturation as a function of flux for water with 30 / 40 sands. It shows an overshoot flux of 2.13×10^{-6} m / s. [DiCarlo, 2004]

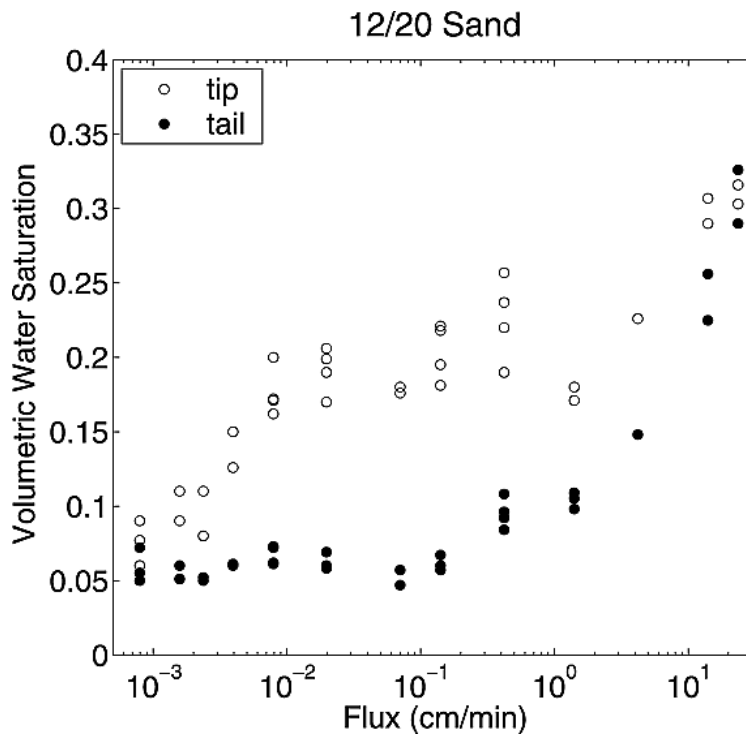


Figure 4 – 9 Measured tip and tail saturation as a function of flux for water with 12 / 20 sands. It shows an overshoot flux of 1.67×10^{-7} m / s. [DiCarlo, 2004]

Figure 4 - 9 plots the tip and tail saturations versus flux for initially dry 12/20 sand. In this case, “the saturation overshoot region is larger (from roughly 0.001 to 15 cm/min) than seen for 30/40 sand. In addition, the tips are more unsaturated than in 30/40 sand.”[DiCarlo 2004] Figure 4 - 10 plots the tip and tail saturations versus flux for initially dry 20/30 sand.

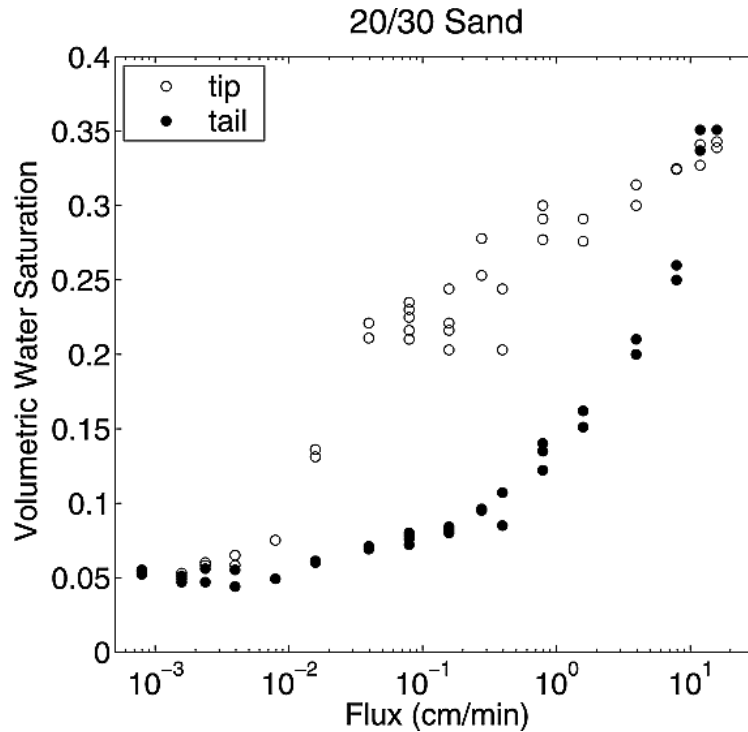


Figure 4 – 10 Measured tip and tail saturation as a function of flux for water with 20 / 30 sands. It shows an overshoot flux of 5.45×10^{-7} m / s. [DiCarlo, 2004]

Figure 4 – 11 shows the measured saturation overshoot as a function of flux for 50 / 70 sand. Over a one order of magnitude flow regime changes from sharp to diffuse.

We also define the tip length as the distance from the infiltration front to where the saturation is halfway between its initial value and the tail value. If the difference between the tip and tail saturation is below the noise level, no tip length is recorded.

Table 4 – 1 shows the complete set of data for the different infiltrating fluids and different media.

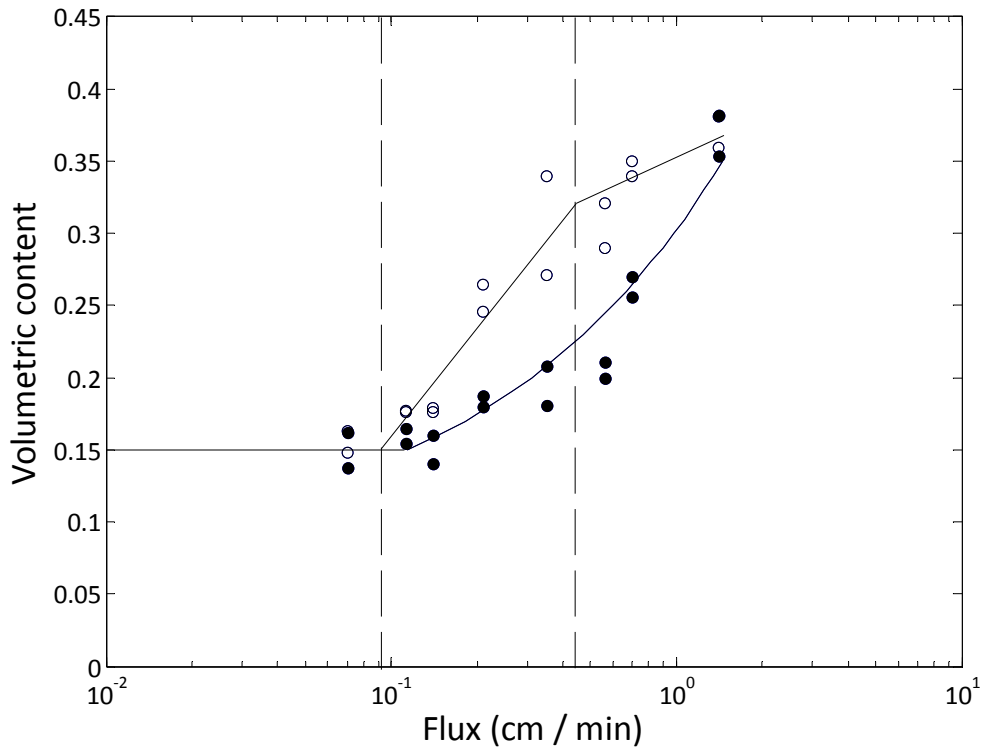


Figure 4 – 11 Measured tip and tail saturation as a function of flux for water with 50 / 70 sands. It shows an overshoot flux of $1.67 \times 10^{-5} \text{ m / s}$.

Table 4 – 1: Measured overshoot flux, transition flux, and tip length

	Overshoot flux (m/s)	Transition flux (m/s)	Tip length* (m)
Water (30/40)	2.13×10^{-6}	4.65×10^{-5}	0.105
Methanol	7.35×10^{-6}	2.17×10^{-5}	0.053
Ethanol	2.05×10^{-6}	2.59×10^{-5}	0.063
1 – Propanol	1.96×10^{-6}	1.27×10^{-5}	0.063
Hexane	1.13×10^{-5}	1.17×10^{-4}	0.041
Octane	6.13×10^{-6}	7.76×10^{-5}	0.05
Decane	3.68×10^{-6}	9.63×10^{-5}	0.063
Water (12/20)	1.67×10^{-7}	1.12×10^{-5}	0.05
Water (20/30)	5.45×10^{-7}	2.65×10^{-5}	0.087
Water (50/70)	1.67×10^{-5}	6.12×10^{-5}	0.142

*The tip length measured at $2.33 \times 10^{-4} \text{ m / s}$ infiltration flux.

The results can be summarized as followed.

1 – As a function of flux, all fluids show three regions separated by two fluxes: an overshoot flux (above which overshoot occurs), and a transition flux (above which the tip saturation is constant).

2- The transition and overshoot flux decrease with an increasing molecular weight for both alcohols and alkanes.

3 – Overshoot flux decreases rapidly by increasing the grain size.

4 – By increasing the molecular weight for both alcohols and alkanes, the tip length increases.

4 – 2: Theoretical Evidence

A semi-continuum argument to estimate the overshoot flux was applied. We hypothesize that if the continuum equations predict that the saturation changes by an amount greater than S_s (some saturation) over a distance equal to a grain size, the continuum description will be inadequate and discrete pore filling rules will come into play. This is depicted in the Fig. 4 – 12.

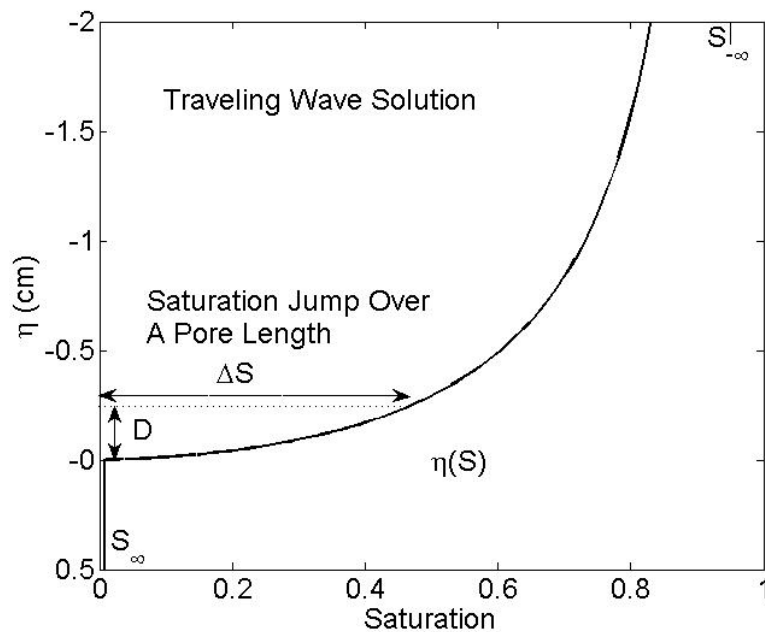


Figure 4 - 12 Saturation profile as a function of η , Richard's equation is inadequate in describing the fluid behavior if Δs is higher than snap off saturation

Is the front sharp or diffuse at the pore scale. We will take the pore scale distance is given by D , the average grain size. The initial saturation is S_0 .

The front will be diffuse if snap-off can occur at least a few grains ahead of the main wetting front. This will allow the saturation at the front to rise continuously through a

combination of snap-off and collective pore filling processes. This snap-off is allowed as the conduction through the wetting layers. The following analysis of the overshoot behavior is based upon the qualitative analysis of Lenormand and Zarcone.

For a diffuse front, there should be enough saturation a couple of grains ahead of the front ($S(z_f+2D)$ where D is the grain size) to allow enough layer flow to snap off a few throats and pores. For a sharp front, this saturation ($S(z_f+2D)$) is not enough to allow snap off, and the pores can only fill collectively at the front (Simply the fluid movement through the layer cannot match the speed of front). The exact amount of saturation required to elicit snap off is unknown (though it may be dependent on the grain shape), let us just label it S_s for snap-off saturation. Thus we are looking for a flux for which $S(z_f+2D) = S_s$.

We solve for $S(z_f+2D)$ using the traveling wave nature of the advancing front. We start with the conservation equation,

$$\phi \frac{\partial S}{\partial t} = -\frac{\partial q}{\partial z} \quad (4-2)$$

Applying the traveling wave variable transformation $\eta = z - vt$, and integrating gives us

$$\phi v(S - S_0) = q - q_0 \quad (4-3)$$

For sake of brevity let us assume that the initial saturation and the initial flux are zero.

Using the Darcy-Buckingham equation for the flux gives us,

$$\phi v S = \frac{K k_r(S)}{\mu} \left(\frac{dP_c}{dS} \frac{dS}{dz} + \rho g \right) \quad (4-4)$$

Now use Leverett scaling for the capillary pressure

$$P_c = \sigma \sqrt{\frac{\phi}{K}} J(S) \quad (4-5)$$

Ahead of the front $S < S_s$, and for these low saturations we can ignore the gravitational term (the pull from capillary forces is greater than the pull from gravity). This gives

$$\phi v S = \frac{\sigma \sqrt{K \phi}}{\mu} k_r(S) J'(S) \frac{dS}{dz} \quad (4-6)$$

For a similar medium, the term $k_r(S) J'(S)$ has all of the saturation dependence (non-linearity), and does not depend on the size of the medium, nor any of the fluid properties.

We can finally solve for S as a function of z by integrating

$$z - z_F = \frac{\sigma}{\mu v} \sqrt{\frac{K}{\phi}} f(S, S_0), \quad (4-7)$$

where

$$f(S, S_0) = \int \frac{k_r(S) J'(S)}{S} dS, \quad (4-8)$$

Finally, the transition between a sharp and a diffuse front is given by $S = S_s$ @ $z = z_f + D$, or when

$$D = \frac{\sigma}{\mu v} \sqrt{\frac{K}{\phi}} f_s, \quad (4-9)$$

where $f_s = f(S_s, S_0)$ is a constant which is very difficult to explicitly calculate due to a) the unknown snap-off saturation, b) the unknown initial saturation, and c) the unknown constitutive curves at very low saturation. The velocity of the front is observed experimentally to vary linearly with the applied flux.

4 – 3: Discussion

As mentioned in the introduction, saturation overshoot is forbidden in standard model with nonmonotonic pressure saturation and relative permeability curves only depend on saturation. Instead, we hypothesize that different pore filling mechanisms dominate below and above the overshoot flux; therefore we can capture the saturation overshoot by discrete model of saturation. This hypothesis agrees with Lenormand and Zarcone [*Lenormand and Zarcone, 1984*] experiments, which suggest that the real physics is happening at the pore-scale and not the continuum scale. The pore-scale physics changes with rate; it becomes harder to fill pores ahead of the front with the snap-off mechanism, only leaving the piston-like mechanism that tends to oversaturate the medium. In essence, there is a competition between the flux through the wetting layers, and the flux of the main wetting front, and that the observed overshoot flux is the flux for which these are equal.

The flux through the wetting layers depends on a) the creation of the layers; b) the swelling and eventual size of the layers; c) the viscous transport through the layers; and d) the capillary pressure required for snap-off.

As these are serial processes, the slowest link will likely be the controlling factor. We attempt to find the slowest link by observing how the overshoot flux varies as a function of the fluid parameters. The most important fluid parameters are likely to be a) the viscosity, b) the miscibility with water, c) the surface tension, d) the vapor pressure, and e) density.

First, we consider the viscosity of the fluid. For an equivalent pressure drop and equivalent layers, the flux through the layers depends inversely on the viscosity [*Dong*

and Chatzis, 1995; Patzek and Kristensen, 2001; Ransohoff and Radke, 1988]. Thus in Fig. 4 – 13 we plot the overshoot flux versus the inverse of the viscosity for all seven fluids used for 30 /40 sands. Figure 4 – 13 shows a strong linear correlation between the overshoot flux and inverse of the fluid viscosity, which is also, goes through zero. Clearly, the viscosity of the fluid plays a key role in determining the overshoot flux. For this 30/40 sand, we observe that the overshoot flux is fit well by

$$q_{over} = 3 \times 10^{-9} / \mu \quad (4 - 10)$$

where the flux is in m/s, and the viscosity is in Pa. s.

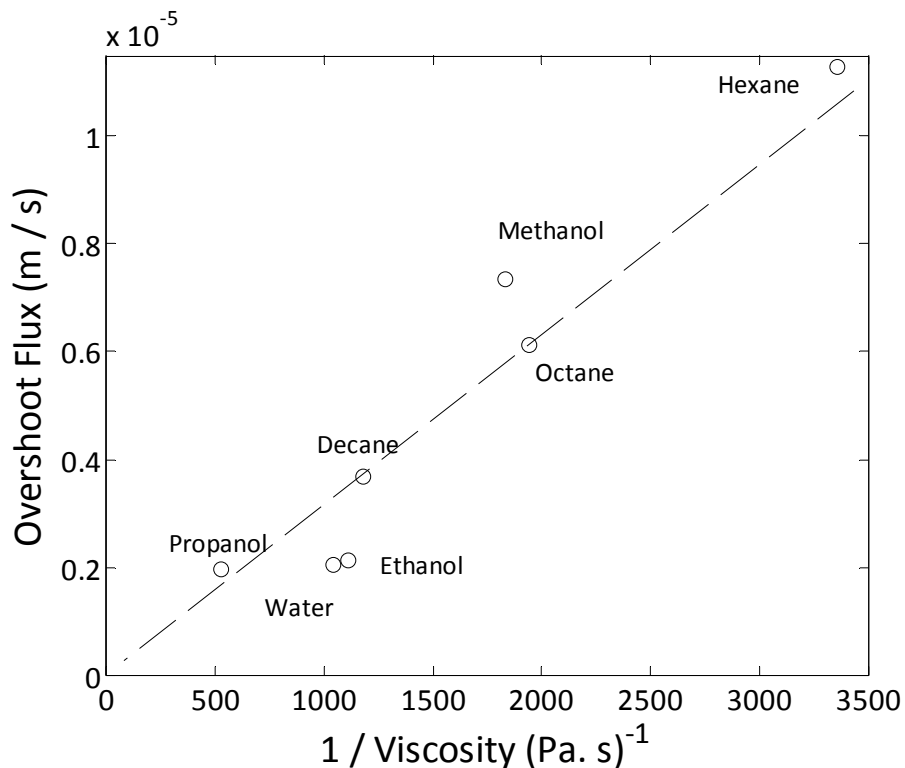


Figure 4 – 13 Measured overshoot flux versus viscosity for all fluids both alcohols and alkenes. The overshoot flux shows an inverse dependence on viscosity.

Second, we consider the miscibility of the invading fluid with water. This may be important in the formation of layers, as even though the sand was packed dry, the sand is in contact with the atmosphere and will pick up microscopic layers of adsorbed water. If the invading fluid is miscible with water, it will mix with these initial water layers, and

the layers can swell from there. If the invading fluid is immiscible, it will have to form its layers on top of the water phase. From Fig. 4 – 13 alcohols that are miscible with water fall on the same line with alkanes that are immiscible. Thus the miscibility seems to play little or no role in the overshoot flux, and thus the diffuseness of the interface. However, additional experiment with initial water saturation is required to clarify the difference between the layer flow (for alcohols) and film flow (for alkenes).

Third, we consider the surface tension of the invading fluid. A larger surface tension will lead to greater capillary forces, and increases the capillary entry pressure of each pore. This will change the ratio of the capillary forces to viscous forces which is normally expressed by the capillary number,

$$N_{Ca} = \frac{\mu v}{\sigma} \quad (4-11)$$

where v is the velocity of the front, μ is the viscosity, and σ is the surface tension. The capillary number has been found to control the capillary desaturation curve [Stegemeier, 1974], which is another displacement process which deals with sharp and diffuse fronts with the sharp fronts leaving behind less non-wetting phase. The question then is: does the capillary number control the sharp and diffuse fronts when it comes to overshoot? If the capillary number does control the process than the overshoot flux should be at the same capillary number for the different fluids. Calling N_{Ca}^* the capillary number at which the front changes from sharp to diffuse, equation 6 - 22 can be inverted to get the overshoot velocity v_{over} , or equivalently, the velocity above which overshoot occurs,

$$v_{over} = \frac{\sigma N_{Ca}^*}{\mu} \quad (4-12)$$

The overshoot velocity can be found from the overshoot flux as the saturation profile translates downward at a constant velocity (it is a traveling wave), and thus the main wetting front velocity is this same constant velocity and is given by

$$v = \frac{q}{\phi S_{tail}} \quad (4 - 13)$$

where q is the applied flux, S_{tail} is the tail saturation and ϕ is the porosity. The data shows that for 30 / 40 sand the tail saturation is almost constant with flux at the overshoot flux for all the fluids tested (see Figs 4 – 2 through 4 – 8), and has a value of roughly $S_{tail} \approx 0.25$. Thus, if the capillary number controlled the overshoot, the overshoot flux would be related to the fluid properties through

$$q_{over} = \phi S_{tail} \frac{\sigma N_{Ca}^*}{\mu} \quad (4 - 14)$$

Figure 4 – 14 shows the overshoot flux versus the surface tension divided by viscosity.

The overshoot flux does not fit as well with using the ratio of surface tension and viscosity rather than just the simple inverse viscosity seen in Fig. 4 – 13. But only the water shows a great discrepancy, as unfortunately all of the alkanes and alcohols have pretty much the same surface tension. Testing the dependence of the overshoot fluxes on the surface tension is more difficult than testing the dependence on the viscosity. It is straightforward to find fluids with a range of viscosities, but almost all non-polar liquids have approximately a surface tension of 20×10^{-3} N/m at room temperature and pressure. This work is being done by using different mixtures of water and alcohol with wide range of viscosity and surface tension. The surface tension is controlled between 70×10^{-3} and 20×10^{-3} N/m.

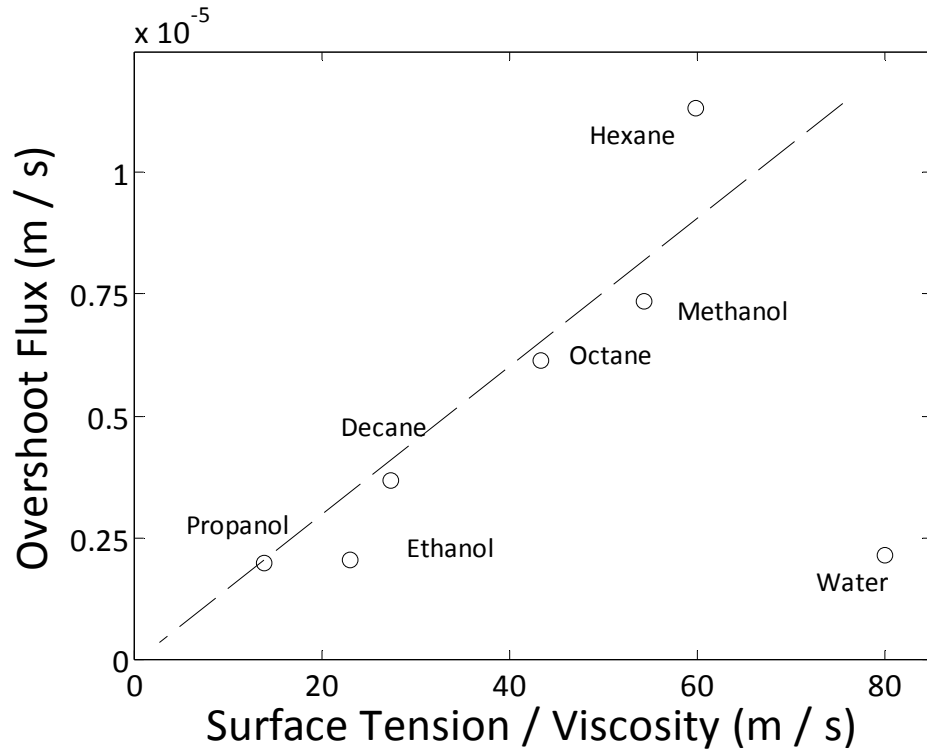


Figure 4 – 14 Measured overshoot flux as a function of surface tension / viscosity. It shows a linear relationship, except for water, between overshoot flux and surface tension / viscosity.

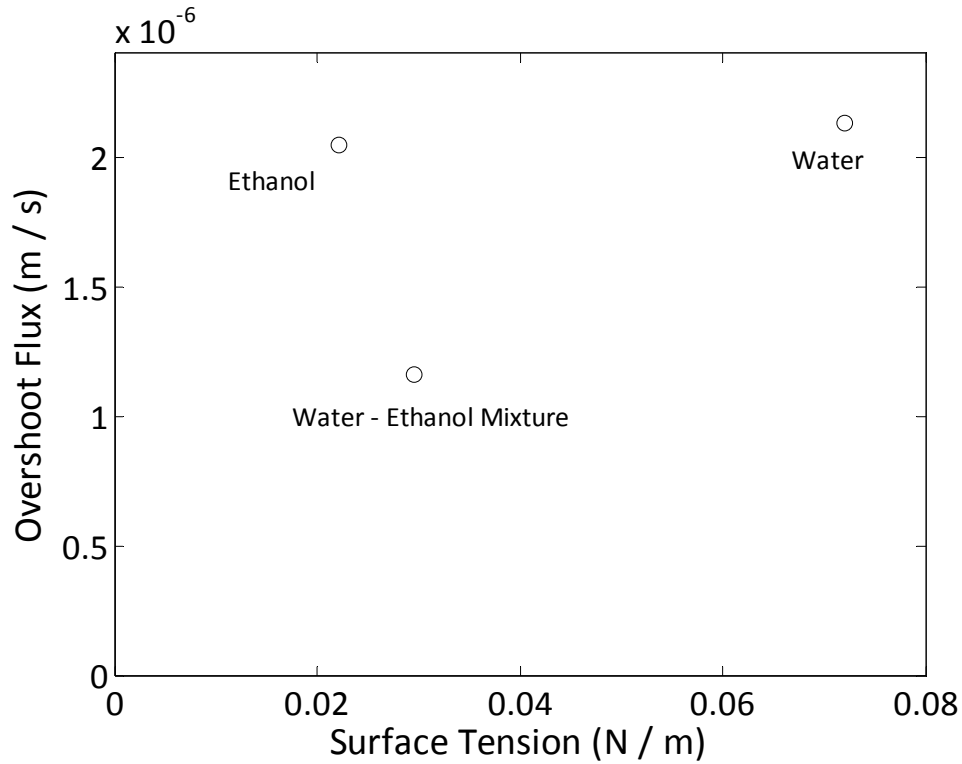


Figure 4 – 15 Measured overshoot flux as a function of surface tension. It shows overshoot flux is independent of surface tension.

Figure 4 – 15 and 4 – 16 show the saturation overshoot as a function of surface tension and surface tension / viscosity for water, Ethanol, and 50 – 50 mixture of water and ethanol respectively. The mixture viscosity is 2.2×10^{-3} pa. s; therefore, the lower overshoot flux for the mixture is because of its higher viscosity. As it shown in the fig. 4 – 14 and 4 –16 the overshoot flux is independent of surface tension. This new set of experiment agrees well with the previous data and shows the dependency of overshoot flux on inverse of viscosity.

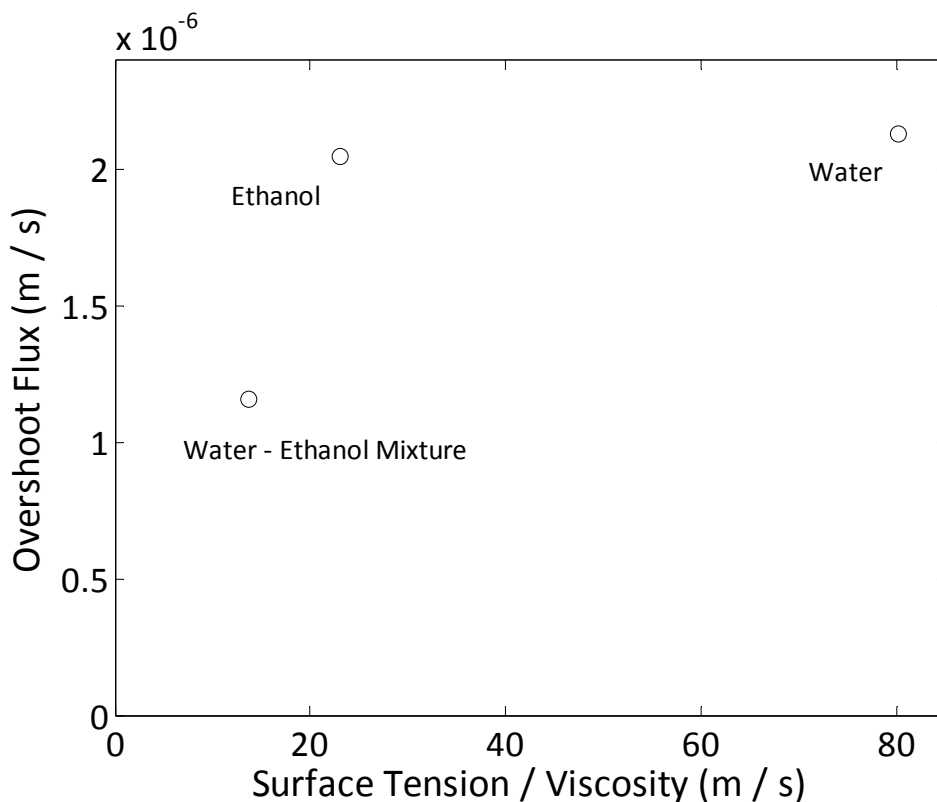


Figure 4 – 16 Measured overshoot flux as a function of surface tension / viscosity. It shows overshoot flux is independent of surface tension.

Fourth, we consider the vapor pressure of the invading fluid. Vapor transport may be a key process in the initial formation of the wetting layers before the front [de Gennes, 1985]. Figure 4 - 17 shows the overshoot flux versus vapor pressure for all 7 fluids.

Though there is some correlation in that the fluids with higher vapor pressures tend to have higher overshoot fluxes, this correlation is most likely to be caused by the fact that fluids with the highest vapor pressure have the lowest viscosities. Qualitatively, this can be noticed by looking in particular at decane. Decane has by far the lowest vapor pressure, but has a higher overshoot flux than ethanol and water.

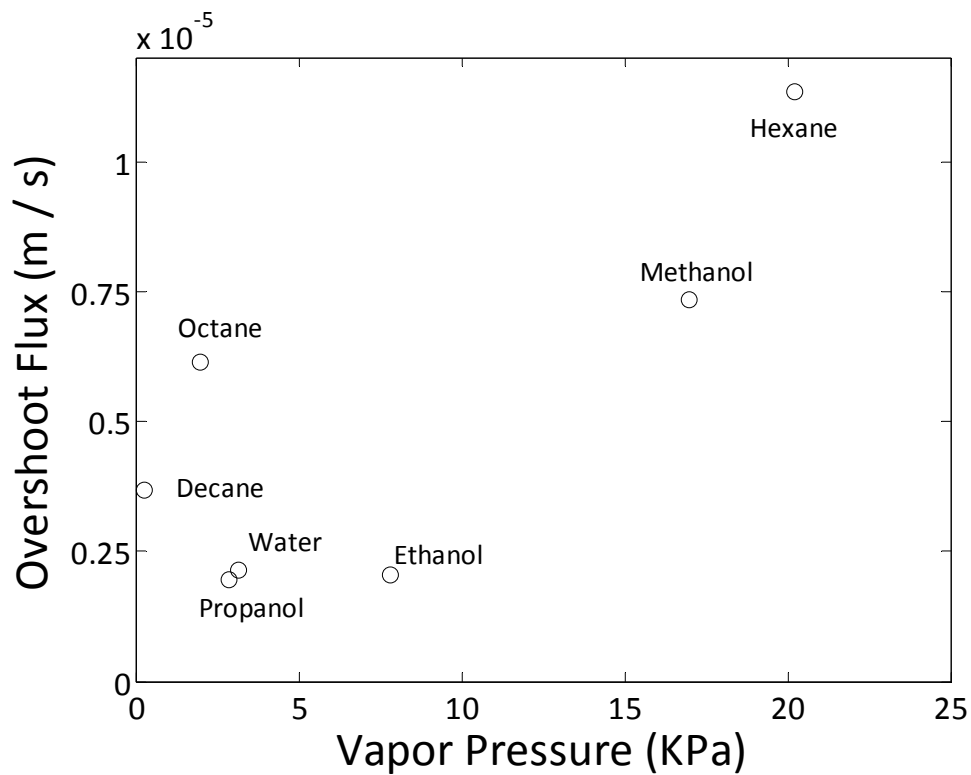


Figure 4 – 17 Measured overshoot flux as a function of vapor pressure for all fluids both alcohols, alkenes and water. There is a weak dependence between vapor pressure and overshoot flux.

We can also estimate the role of vapor transport using Fick's law and some simple estimates. Vapor flow through the permeable medium by diffusion can be expressed as

$$q_{vap} = -\rho_v \frac{\phi}{\tau} D_{vap-air} \frac{dy}{dz} \quad (4 - 15)$$

where ρ_v is the density of vapor phase, τ is the tortuosity of the permeable medium, $D_{vap-air}$ is the diffusion coefficient of vapor in air, and y is the mole fraction in the vapor phase. Mole fraction can be expressed as the ratio of vapor pressure to the atmospheric pressure. Vapor pressure over the concave liquid meniscus is less than the vapor pressure over a flat water surface. The relationship between the vapor pressure and radius of curvature of the interface is describe by the Kelvin's equation [Bear, 1972]

$$P^{vap} = P_{sat} e^{-P_c / \rho_L RT} \quad (4-16)$$

where P^{vap} is the vapor pressure over the concave meniscus, and P_{sat} is the vapor pressure over the flat surface. The vapor transport equation is therefore,

$$q_{vap} = -\rho_v \frac{\phi}{\tau} D_{vap-air} \frac{P_{sat}}{P_a} e^{-P_c / \rho_L RT} \left(-\frac{1}{\rho_L RT} \frac{dP_c}{dS} \frac{dS}{dZ} \right) \quad (4-17)$$

We use van Genuchten [van Genuchten, 1980] model for capillary pressure curve,

$$\Rightarrow \frac{dP_c}{dS} = \frac{1}{mn\alpha} S^{-1/m} = C_0 S^{-\beta} D^{-1} \sigma \quad (4-18)$$

The vapor transport can be therefore be estimated through,

$$q_{vap} = \rho_v \frac{\phi}{\tau} D_{vap-air} \frac{C_0 S^{-\beta+1} D^{-2} \gamma M_w P_{sat}}{\rho_L RT (\beta-1) P_a} e^{-P_c / \rho_L RT} \quad (4-19)$$

where C_0 and β are the van Genuchten constant and obtain from table 1. D is the particle diameter and M_w is the molecular weight of the injecting fluid. Figure 4 – 18 shows the measured overshoot flux as a function of calculated vapor transport, which shows that the calculated vapor transport underestimate the overshoot flux six orders of magnitude. Both the experimental results and the calculations show that the lack of dependence on vapor pressure suggests that vapor transport plays little or no role in the dynamics of the front.

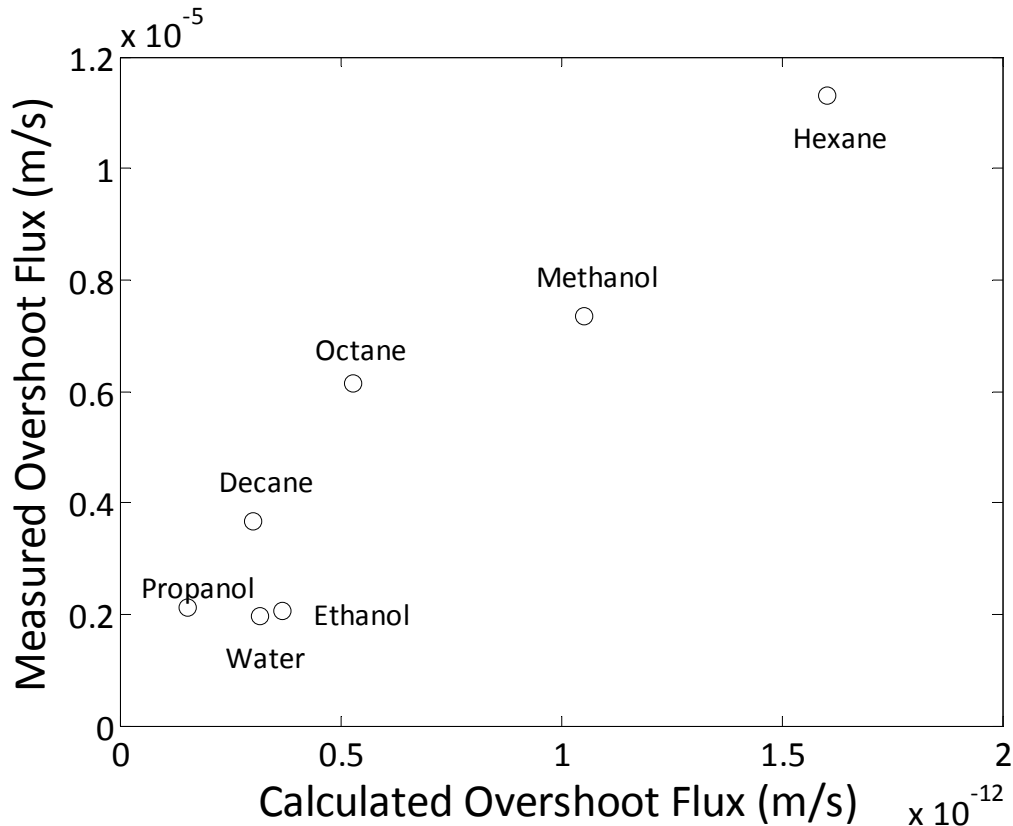


Figure 4 – 18 Measured overshoot flux as a function calculated overshoot flux. The vapor transport model underestimates experimental behavior.

Fifth, we analyze the gravitational forces. Lenormand and Zarcone [1984] explain the transition between sharp and diffuse front in the horizontal micromodel as a competition between capillary and viscous forces. In our vertical experiments, gravitational forces may play a role at the pore scale. Since density is the driving force for layer flow, and viscosity is the resisting force, in Figure 4 – 19 we show the overshoot flux as a function of density divided by viscosity. Figure 4 - 19 is similar to Fig. 4 – 14. As in the case for capillary forces (Fig 4 – 9), the variation of the densities of the fluids is much less than the variation in viscosities, and it is difficult to deduce the gravitational component using these fluids. We are planning to perform experiments in different geometries to greater elucidate the effect of density.

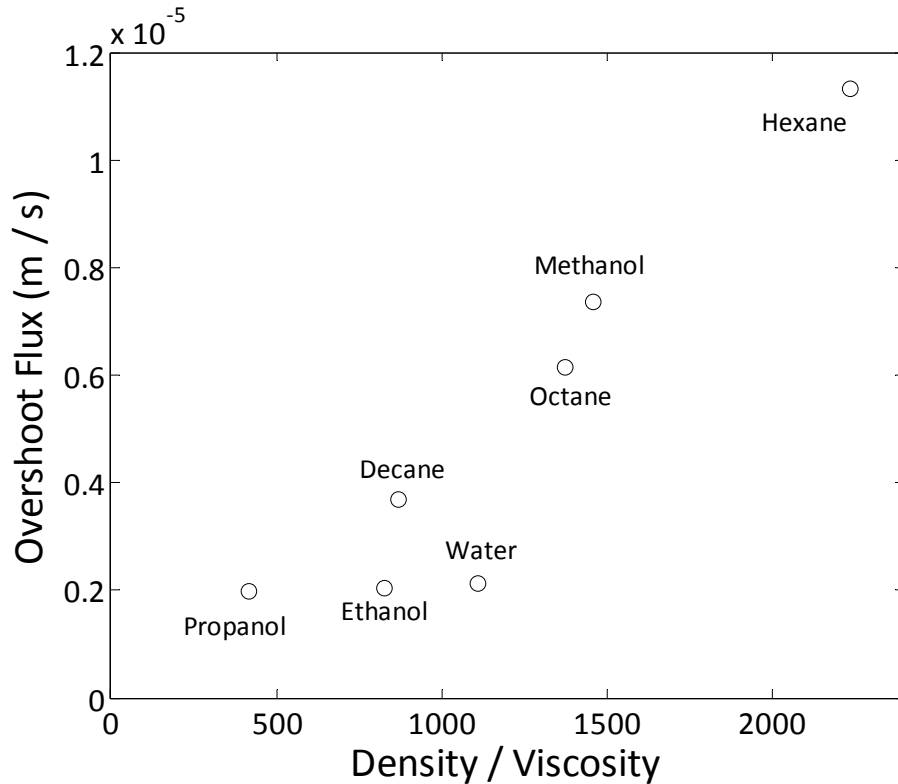


Figure 4 - 19: Measured overshoot flux as a function of density / viscosity for all fluids both alcohols, alkenes and water. There is a weak dependence between density / viscosity and overshoot flux.

Sixth, we consider the grain size. From observations in their micromodels, [Lenormand and Zarcone, 1984] Lenormand and Zarcone proposed that the pore-scale processes that affect the CDC are the competition between snap-off (which needs layer flow) and piston-like (which is collective). In this study, we offered that the same mechanisms may be taking place [DiCarlo, 2004]. The capillary desaturation curve is independent of the grain size, however, we observe the large dependency of the overshoot flux and therefore the transition between the sharp and diffuse front with grain size. Figure 4 – 20 shows the overshoot flux as a function of grain size. We observe that the overshoot flux is scale as D^{-3} . This can be explained as the volume of the liquid required for snap off scale as the D^3 .

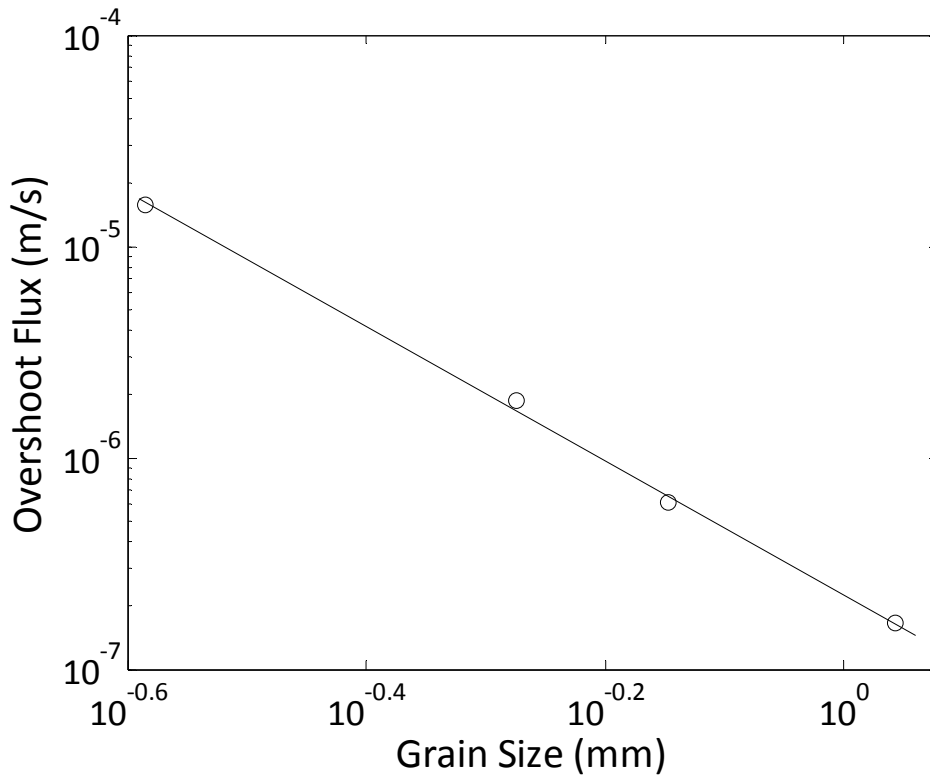


Figure 4 - 20 Measured overshoot flux as a function of grain size for water. There is a linear dependence in log – log plot for overshoot flux as a function of grain size. Overshoot flux scale as D^3 .

Plotting the hydraulic conductivity along with the overshoot flux in Fig. 4 – 21 suggest that at the intersection of these two lines (sand with grain size of 0.108 mm) no saturation will be observed. Currently we are testing whether the saturation overshoot occur with the 100/140 sand. This is more difficult than testing larger grain size. Since analyzing the saturation using light transmission and making the calibration column are more challenging.

Finally, we consider the tip length. The tip length is related to the hysteresis in the medium and corresponds to the capillary pressure difference. Figure 4 - 22 shows the tip length versus the ratio of the surface tension to the density of the infiltrating fluid. This follows a straight line for all the fluids tested. This is unsurprising as the tip length is the low-pressure vertical part of the pressure-saturation curve divided by the gravitational

gradient. Leverett scaling predicts that the P-S curve should scale with the surface tension, and the gravitational gradient scales with the fluid density.

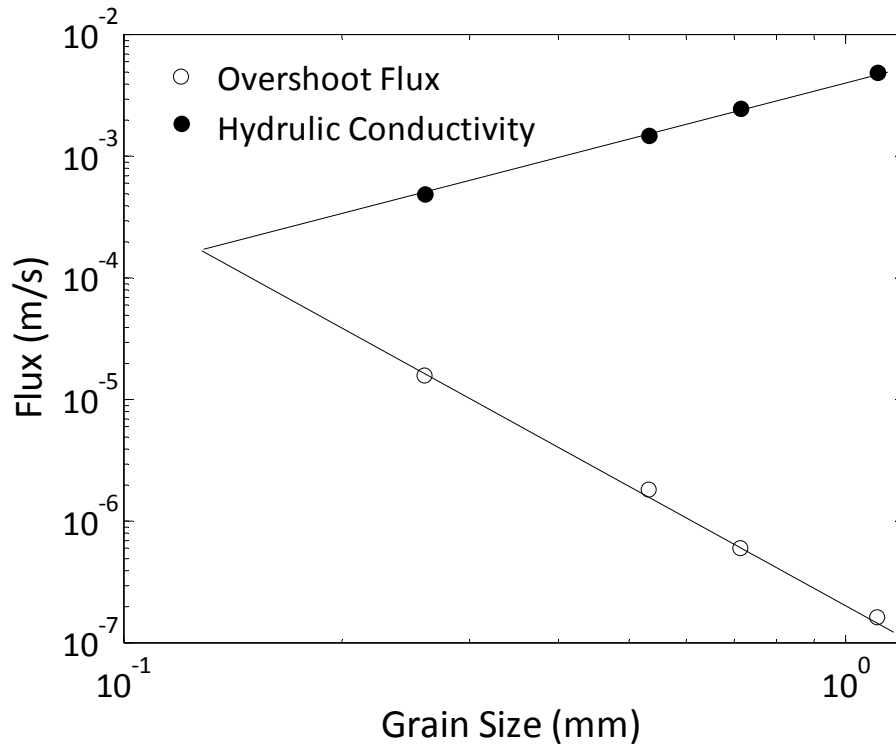


Figure 4 – 21 Measured overshoot flux and hydraulic conductivity of water as a function of grain size. The intersection of these two lines is at 0.108 mm and predicts the overshoot flux as 0.186×10^{-4} .

It is somewhat surprising that the surface tension plays a role in the tip length, but does not appear to play a role in the overshoot flux. Again, this discrepancy is in the process of being studied.

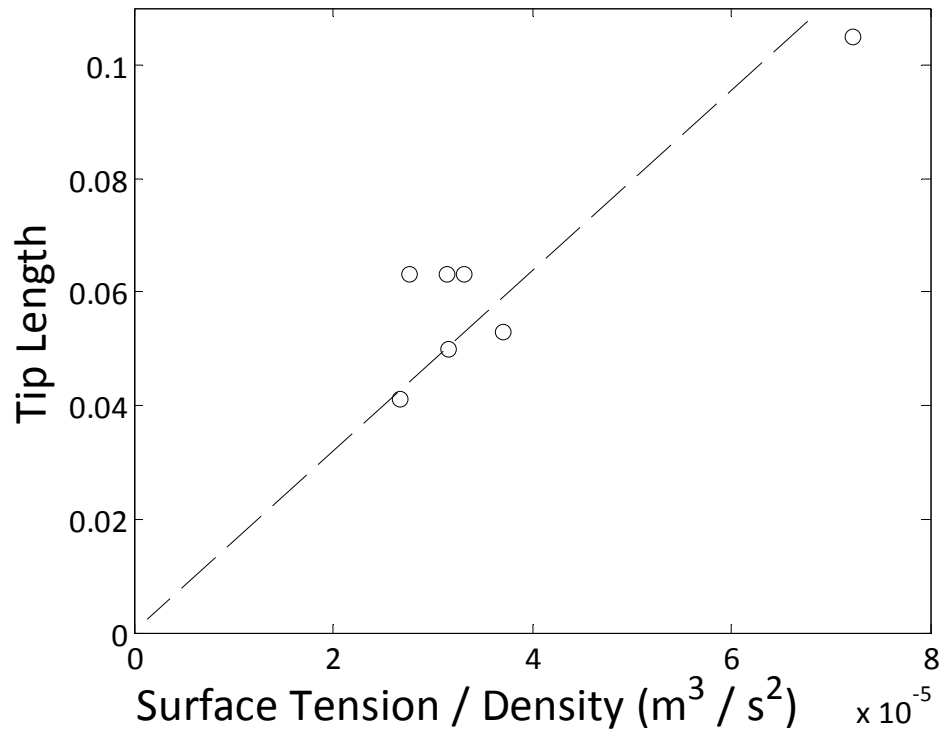


Figure 4 – 22 Measured tip length as a function of surface tension / density for all fluids: alcohols, alkanes and water. The tip length was measured from the infiltration front to where the saturation is halfway between its initial value and the tail value. There is a linear dependence between tip length and surface tension / density.

4 – 4: Proposed Model

As we mentioned in the introduction, saturation overshoot cease when certain amount of water saturation is available ahead of main wetting front. This saturation could be only achieved by layer flow.

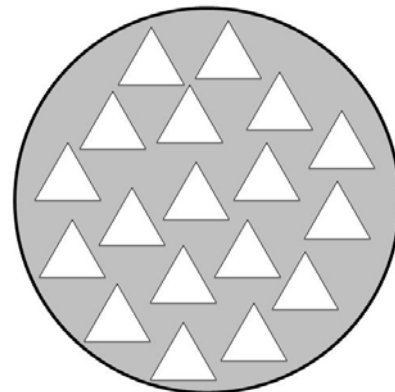


Figure 4 – 23 Flow through a triangular duct with Constant cross-section area

Irmay (1958) proposed a method to estimate viscous flow through a pack of spheres as shown averaging the Navier–Stokes Equations. Integrating over the entire cross section results in Poisson’s equation.

$$\frac{\partial^2 v_z}{\partial x^2} + \frac{\partial^2 v_z}{\partial y^2} = -\frac{1}{\mu} \frac{\Delta \varphi}{L}, \quad (4-20)$$

From the momentum balance flow through the triangular duct can be determined as follows,

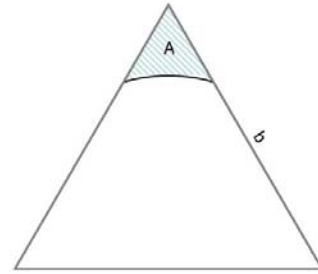
$$v_z = \frac{\sqrt{3}}{6b} \left(y + \frac{b}{2\sqrt{3}}\right) \left(y + \sqrt{3}x - \frac{b}{\sqrt{3}}\right) \left(y - \sqrt{3}x - \frac{b}{\sqrt{3}}\right) \frac{\Delta \varphi}{\mu L}, \quad (4-21)$$

From the Eq. 4 -21 Poisson’s law yields to

$$q = \frac{\sqrt{3}b^4}{320} \frac{\Delta \varphi}{\mu L} \quad (4-22)$$

Eq. 4 -22 describes flow through the entire triangular area. Here we try to estimate the flow through a layer (A) as it shows in Fig 4 – 24.

Figure 4 – 24 Flow through a Layer ahead of the main wetting front



The area open to flow can be calculated from the

Eq. 4 – 23

$$A = \frac{1}{12} D^2 \left(\frac{\cos(\beta + \theta) \cos \theta}{\sin \beta} - (90 - \beta - \theta) \left(\frac{2\pi}{360} \right) \right) \quad (4-23)$$

Where θ is the contact angle and β is the triangle angle, and D is the grain size. Assuming that $P_c = P_w$ (since the air pressure is constant) and displacement is vertical. Therefore, the flux is equal to

$$Flux = \frac{Cr^4}{80\mu D^2} \left(\frac{\partial P_c}{\partial z} + \rho g \right) \quad (4-24)$$

Where C is equal to $\frac{1}{12} \left(\frac{\cos(\beta + \theta)\cos\theta}{\sin\beta} - (90 - \beta - \theta) \left(\frac{2\pi}{360} \right) \right)$, and r is the layer

thickness. Gravity forces are negligible in compares with capillary forces therefore Eq. 4 – 24 reduce to

$$Flux = C \frac{r^4}{80\mu D^2} \frac{\partial P_c}{\partial z} \quad (4-25)$$

We assume that the required saturation for snap – off has to occur at least a few grains ahead of main wetting front. Here, we use van – Genuchten [*van Genuchten*, 1980] fitting parameter for capillary pressure; partial derivative of capillary pressure with respect to saturation, therefore, is equal to:

$$\Rightarrow \frac{dP_c}{dS} = -C_0 \sigma S^{-\alpha} D^{-1}, \quad (4-26)$$

where C_0 and α are the van genuchten fitting parameters and σ is the surface tension.

Integrating the Eq. 4 -25 yields to

$$Flux = C' \frac{\sigma r^4}{\mu D^4} S^{-\alpha} \quad (4-27)$$

However, saturation is equal to the area of layer divided by the tube area

$$S = \frac{3A}{A_{Tube}} = \frac{Cr^2}{\sqrt{3}/4 D^2} \quad (4-28)$$

Therefore the flux is equal to

$$Flux = C' \frac{\sigma r^4}{\mu D^4} S^{-\alpha} = C'' \frac{\sigma r^4}{\mu D^4} \cdot \left(\frac{D^2}{r^2} \right)^\alpha \quad (4-29)$$

Figure 4 -25 shows the estimated flux ahead of main wetting front for 30 / 40 sand.

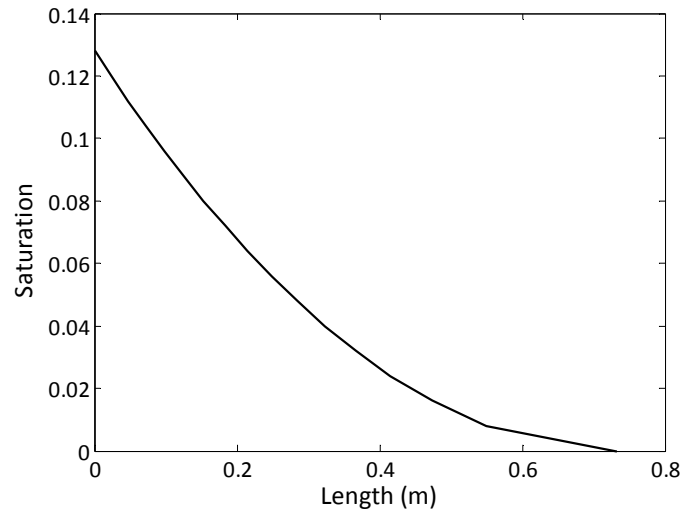


Figure 4 -25 Estimated flux ahead of the main wetting front for water in 30 / 40 sand.

Chapter 5: Summary and Conclusion

Vertical displacement of the wetting phase by a non wetting phase in the 1D scale, shows a non-monotonic saturation profile with high saturation at the front (tip) followed by a lower saturation behind the front (tail). This behavior is suggested to be a cause of preferential flow in the 3D scale. We also hypothesize that the saturation overshoot in the core scale corresponds to the sharp front in the pore scale. We conduct a series of displacement experiments to study the dynamics of the overshoot and front sharpness as a function of applied flux and fluid properties by using fluids varying in viscosity, vapor pressure, and surface tension. We found that the transition flux between the two regimes depends linearly on the viscosity of the invading fluid, and we model the front dynamics using a semi-continuum model. Determination of the displacement efficiency and sweep efficiency under different flooding scenarios is crucial for modeling enhanced hydrocarbon recovery.

It still remains unclear when the saturation profile is uniform, with high residual oil saturation and high sweep efficiency and *exactly* when the saturation overshoot occurs. Previous experiments show that there is an overshoot flux above where this flux saturation overshoot occurs, and below where saturation overshoot is ceases.

To understand the physics behind the saturation overshoot. We develop an experimental system ideal for analyzing the pore scale collective or individual filling mechanisms. This is combined with a semi-continuum model that is used to predict whether the fluid front is sharp or diffuse. Finally, we analyze the parameters that can affect the overshoot flux. This includes vapor pressure, surface tension, density, and viscosity.

In summary, all of the fluids tested show the same saturation overshoot behavior as a function of flux, with only the magnitude of the overshoot flux changing from fluid to fluid. The overshoot flux varies inversely with viscosity and shows little dependence on surface tension, miscibility, and vapor pressure of the infiltrating fluid. These results imply that the slowest link in moving flow ahead of the front is the flow through the wetting layers; the formation or swelling of the layers plays little or no role. Thus, the transition between a sharp and a diffuse front is controlled only by the viscosity. These results only apply to how this transition is affected by fluid properties; previous measurements have shown a strong dependence on the medium size, type, and initial fluid saturation. This data set along with the previous data sets will help elucidate the important physics at saturation fronts and its relation to larger scale flows.

In conclusion, capillary desaturation curve can qualitatively explain the transition between sharp and diffuse front. As it demonstrated in the CDC we observe that the transition between sharp and diffuse (overshoot flux) shows a strong linear correlation with inverse of the invading fluid viscosity, which also, goes through zero. However, unlike the CDC, the overshoot flux does not fit as well with the ratio of surface tension and viscosity. This behavior is also observed in polymer flooding. Huh and pope [2008] observed that the polymer flood can reduce the residual oil saturation. Capillary number is also independent of the grain size, which we observed a large dependency on the grain size. Therefore, the capillary desaturation curve is not the solely controlling factor in transition between sharp and diffuse front.

NOMENCLATURE

P_c	: Capillary pressure, [Pa]
k	: Permeability, [md]
S_N	: Normalized wetting phase saturation, [fraction]
S_w	: Wetting phase saturation, [fraction]
S_{wr}	: Residual wetting phase saturation, [fraction]
S_{mwr}	: Residual non-wetting phase saturation, [fraction]
k_{rw}	: Wetting phase relative permeability, [fraction]
k_{mwr}	: Non-wetting phase relative permeability, [fraction]
$S_{w,irr}$: Irreducible water saturation, [fraction]
N_{ca}	Capillary Number, [dimensionless]
v	Velocity, [m / s]
R, r	Pore Radius, [mm]
l	Characteristic Length, [m]
q	Volumetric Flux, [m/s]
Q	Volumetric Flow Rate, [m ³ /s]
N_{cb}	Capillary – Bond Number [dimensionless]
I	Light Intensity
D, d	Grain Size [mm]
J	Leverett J – Function

R_h	Hydraulic Radius,[m]
$D_{vap-air}$	Diffusion Coefficient, [m ² /s]
M_w	Molecular Weight, [kg / kgmol]
μ	Viscosity, [pa. s]
σ	Surface Tension [N/m]
θ	Contact Angle
ρ	Density, [kg / m ³]
ω	Angular Frequency
ϕ	Porosity, [fraction]
λ	Gravity Potential

ACRONYMS

CDC	: Capillary Desaturation Curve
LTM	: Light Transmission Method

References

- Alvarado, F. A., Grader, A., Karacan, O., and Halleck, P., (2004), Visualization of Three Phases in Porous Media Using Micro Computed Tomography, *Petrophysics Journal*, **45(6)**, 490-498.
- Bauters, T. W. J. and DiCarlo, D.A., (2000), Soil Water Content Dependent Wetting Front Characteristics in Sands, *Journal of Hydrology*, **231-232**, 244-254.
- Bear, J. (1972), *Dynamics of Fluids in Porous Media*, 764 pp., American Elsevier, New York.
- Blunt, M. J., and Scher H., (1995), Pore-level Modeling of Wetting Front, *Physical Review E*, **52**, 6387-6403.
- Culligan, K. A., and Wildenschild, D., (2006), Pore-scale Characteristics of Multiphase Flow in Porous Media: A Comparison of Air-water and Oil-water Experiments, *Adv. Water Resour.*, **29(2)**, 227-238.
- Cueto-Felgueroso, L. and Juanes, R., (2008). "Nonlocal Interface Dynamics and Pattern Formation in Gravity-Driven Unsaturated Flow through Porous Media." *Physical Review Letters* **101(24)**: 244504.
- Cueto-Felgueroso, L. and Juanes, R., (2009). "Stability Analysis of a Phase-field Model of Gravity-driven Unsaturated Flow Through Porous Media." *Physical Review E* **79**: 036301.
- de Gennes, P. G. (1985), Wetting: Statics and Dynamics, *Review of Modern Physics*, **57(3)**, 827-863.
- DiCarlo, D. A. (2004), Experimental Measurements of Saturation Overshoot on Infiltration, *Water Resources Research*, **40**, W04215, doi:04210.01029/02003WR002670.
- DiCarlo, D. A. (2006), Quantitative Network Model Predictions of Saturation Behind Infiltration Fronts and Comparison to Experiments, *Water Resources Research*, **42**, W07408, doi:07410.01029/02005WR004750.
- DiCarlo, D. A. (2007), Capillary Pressure Overshoot as a Function of Imbibition Flux and Initial Water Content, *Water Resources Research*, **43**, W08402, doi:08410.01029/02006WR005550.
- DiCarlo, D. A. (2007). "Advanced Multi Phase Flow", Class notes.
- Diment, G. A., and Watson, K.K., (1985), Stability Analysis of Water Movement in Unsaturated Porous Materials 3. Experimental Studies, *Water Resources Research*, **21(7)**, 979-984.

Dong, M., and Chatzis, I., (1995), The Imbibition and Flow of a Wetting Liquid Along the Corners of a Square Capillary Tube, *J. Colloid Interface Sci.*, **172(2)**, 278-288.

Geiger, S. L., and Durnford D.S., (2000), Infiltration in Homogeneous Sands and a Mechanistic Model of Unstable Flow, *Soil Science Society of America Journal*, **64(2)**, 460-469.

Glass, R. J., and Oosting, G.H.,. (1989), Mechanism for Finger Persistence in Homogenous Unsaturated Porous Media: Theory and Verification, *Soil Science*, **148(1)**, 60-70.

Hughes, R. G., and Blunt, M.J., (2001), Network Modeling of Multiphase Flow in Fractures, *Adv. Water Resour.*, **24(3-4)**, 409-421.

Lake, L. 1989. *Enhanced Oil Recovery*. Englewood Cliffs, New Jersey: Prentice Hall.

Lenormand, R., and Zarcone, C., (1984), Role of Roughness and Edges During Imbibition in Square Capillaries, *paper SPE 13264* presented at the 59th Annual Technical Conference of the SPE, Houston, TX, September 16-19.

Lenormand, R., and Zarcone, C., (1988), Numerical Models and Experiments on Immiscible Displacements in Porous Media., *J. Fluid Mech.*, **189**, 165-187.

Lu, T. X., and Biggar, J.W., (1994a), Water Movement in Glass Bead Porous Media 1. Experiments of Capillary Rise and Hysteresis, *Water Resources Research*, **30(12)**, 3275-3281.

Lu, T. X., and Biggar, J.W., (1994b), Water Movement in Glass Bead Porous Media 2. Experiments of Infiltration and Finger Flow, *Water Resources Research*, **30(12)**, 3283-3290.

Mogensen, K., and Stenby, E. H., (1998), A Dynamic Two-phase Pore-scale Model of Imbibition, *Transport in Porous Media*, **32(3)**, 299-327.

Niemet, M. R., and Selker, J.S., (2001), A New Method for Quantification of Liquid Saturation in 2D Translucent Porous Media Systems Using Light Transmission, *Adv. Water Resour.*, **24(6)**, 651-666.

Niemet, M. R., Rockhold, M.L., (2002), Relationships Between Gas-liquid Interfacial Surface Area, Liquid Saturation, and Light Transmission in Variably Saturated Porous Media, *Water Resources Research*, **38(8)**, art.1135.

Patzek, T. W., and Kristensen J. G., (2001), Shape Factor Correlations of Hydraulic Conductance in Noncircular Capillaries: II. Two-phase Creeping Flow, *J. Colloid Interface Sci.*, **236(2)**, 305-317.

Ransohoff, T. C., and Radke, C.J., (1988), Laminar Flow of a Wetting Liquid Along the Corners of a Predominantly Gas-occupied Noncircular Pore, *J. Colloid Interface Sci.*, **121(2)**, 392-401.

Rezanezhad, F., Vogel, H.J., (2006), Experimental study of fingered flow through initially dry sand, *Hydrol. Earth Syst. Sci.*, **3**, 2595-2620.

Selker, J., Parlange, J-Y., (1992), Fingered Flow in Two Dimensions: 2. Predicting Finger Moisture Profile, *Water Resources Research*, **28**, 2523-2528.

Stegemeier, G. L. (1974), Relationship of Trapped Oil Saturation to Petro-physical Properties of Porous Media, *paper SPE* presented at Improved Oil Recovery Symposium of Society of Petroleum Engineering of AIME, Tulsa, OK.

Stohr, M., Roth, K., (2003), Measurement of 3D Pore-scale Flow in Index-matched Porous Media, *Experiments in Fluids*, **35(2)**, doi :10.1007/s00348-00003-00641-x.

Stonestrom, D. A., and Akstin K.C., (1994), Nonmonotonic Matric Pressure Histories During Constant Flux Infiltration into Homogeneous Profiles, *Water Resources Research*, **30(1)**, 81-91.

van Genuchten, M. T. (1980), A Closed-form Equation for Predicting the Hydraulic Conductivity of Unsaturated Soils, *Soil Science Society of America Journal*, **44**, 892-898.

Wildenschild, D., and Hopmans, J.W., (2005), Quantitative Analysis of Flow Processes in a Sand Using Synchrotron-based X-ray Microtomography, *Vadose Zone Journal*, **4**, 112-126.

Yao, T., and Hendrickx, J.M.H, (1996), Stability of Wetting Fronts in Dry Homogenous Soils Under Low Infiltration Rates, *Soil Science Society of America Journal*, **60**, 20-28.